2017

Calibration Models and System Development for Compressive Sensing with Micromirror Arrays

Rebecca L. Profeta
Wright State University

Calibration Models and System Development for Compressive Sensing with Micromirror Arrays

A Thesis submitted in partial fulfillment
of the requirements for the degree of
Master of Science in Electrical Engineering

by

REBECCA L. PROFETA
B.E.E., University of Dayton, 2013
B.S.C.E., University of Dayton, 2013

2017
Wright State University

Wright State University
GRADUATE SCHOOL

October 27, 2017

I HEREBY RECOMMEND THAT THE THESIS PREPARED UNDER MY SUPERVISION BY Rebecca L. Profeta ENTITLED Calibration Models and System Development for Compressive Sensing with Micromirror Arrays BE ACCEPTED IN PARTIAL FULFILLMENT OF THE REQUIREMENTS FOR THE DEGREE OF Master of Science in Electrical Engineering.

Joshua Ash, Ph.D.
Thesis Director

Brian D. Rigling, Ph.D.
Chair, Department of Electrical Engineering

Committee on
Final Examination

Joshua Ash, Ph.D.

Arnab Shaw, Ph.D.

Vince Velten, Ph.D.

Barry Milligan, Ph.D
Interim Dean of the Graduate School

ABSTRACT

Profeta, Rebecca L. M.S.E.E., Department of Electrical Engineering, Wright State University, 2017.
Calibration Models and System Development for Compressive Sensing with Micromirror Arrays.

Compressive sensing (CS) is an active research field focused on finding solutions to sparse linear inverse problems, i.e. estimating a signal using fewer linear measurements than there are unknowns. The assumption of signal sparsity makes solutions to this otherwise ill-posed problem possible and has lead to a number of technological innovations such as smaller and less expensive cameras that capture high resolution imagery, low-power radar systems, and accelerated MRI scanners.

In this thesis, we present the development of a hardware CS imaging system using a Digital Micromirror Device (DMD) providing spatial light modulation via an array of micromirrors that can be programmatically controlled to produce automated measurements. Additionally, we develop a number of new DMD-specific calibration models intended to capture the physical attributes of micromirrors and the end-to-end data collection system. Algorithms are derived to fit the calibration models from training data, and resultant CS reconstructions demonstrate a substantial reduction in image estimation error while reducing the number of required measurements by fifty percent, relative to current baseline calibration methods.

List of Symbols

m, n	height and width of DMD mirror array	scalars
K	number of measurements per target	scalar
N	target signal length, $N = mn$	scalar
T	number of calibration targets	scalar
$\boldsymbol{g}$	camera measurement vector	$K \times 1$
$\boldsymbol{x}$	target signal vector	$N \times 1$
$\boldsymbol{\Phi}$	measurement matrix	$K \times N$
$\hat{\boldsymbol{\Phi}}$	estimated (calibrated) measurement matrix	$K \times N$
$\boldsymbol{\phi}_k$	kth measurement operator as a vector	$N \times 1$
$[\boldsymbol{\phi}_k]$	kth measurement operator as a matrix	$m \times n$
$\boldsymbol{P}$	DMD pattern matrix	$K \times N$
$\boldsymbol{p}_k$	kth DMD pattern as a vector	$N \times 1$
$[\boldsymbol{p}_k]$	kth DMD pattern as a matrix	$m \times n$
$\boldsymbol{\theta}$	calibration parameter vector	varies
$\hat{\boldsymbol{\theta}}$	estimate of calibration parameter vector	varies

Contents

List of Figures

List of Tables

Acknowledgment

I would like to take this opportunity to extend my thanks to Dr. Joshua Ash, Dr. Arnab Shaw, and Dr. Vince Velten. This thesis would not have been possible without their support and guidance. I would also like to thank my co-workers at the Air Force Research Labs, Sensors Directorate who provided expertise and helped keep me on track. This paper was cleared for public release on 10 January 2018 by the 88th Air Base Wing as public release number 88ABW-2018-0107.

Introduction

1.1 Compressive Sensing

Compressive sensing (CS) techniques seek sparse solutions to under determined linear systems. This allows sparse signals to be reconstructed from a relatively small number of measurements. For an imaging application, this means that high resolution imagery can be captured with a smaller focal plane array (FPA) or even by a single detector at the cost of taking multiple measurements per image.

For a target signal $\boldsymbol{x}$ of length N, it is assumed that $\boldsymbol{x}$ is either sparse, meaning that the number M of non-zero elements is much less than the signal length ($M << N$), or that $\boldsymbol{x}$ can be represented sparsely in some basis $\boldsymbol{B}$. That is, $\boldsymbol{x} = \boldsymbol{B}\boldsymbol{w}$, where $\boldsymbol{B}$ is a matrix of basis vectors and $\boldsymbol{w}$ are associated weights, most of which are zero. Compressive sensing measurements, $\boldsymbol{g}$, are taken according to a measurement matrix $\boldsymbol{\Phi}$,

$$\boldsymbol{g} = \boldsymbol{\Phi}\boldsymbol{x}. \tag{1.1}$$

In the optical regime, the physical representation of $\boldsymbol{\Phi}$ is referred to as a Spatial Light Modulator (SLM). A SLM can be either reflective or transmissive. A reflective SLM reflects known portions of the target signal towards the detector. A popular choice of reflective SLM is a digital micromirror device (DMD) which contains an array of controllable micromirrors used to reflect portions of the target signal towards or away from the detector.

A transmissive SLM controls the incident light on the target illuminating known portions. The reflective or transmissive SLM moves through a series of patterns to randomly sample the target signal in a controlled manner. Each row of the measurement matrix, $\mathbf{\Phi}$, is a single SLM pattern used to sample the target signal $\boldsymbol{x}$ which gives a corresponding measurement, g_k,

$$\underbrace{\begin{bmatrix} g_1 \\ g_2 \\ \vdots \\ g_K \end{bmatrix}}_{K\times 1} = \underbrace{\begin{bmatrix} & \boldsymbol{\phi_1}^T & \\ & \boldsymbol{\phi_2}^T & \\ & \vdots & \\ & \boldsymbol{\phi_K}^T & \end{bmatrix}}_{K\times N} \underbrace{\begin{bmatrix} x_1 \\ x_2 \\ \vdots \\ \vdots \\ \vdots \\ x_N \end{bmatrix}}_{N\times 1}, \tag{1.2}$$

and each individual measurement, g_k, is the inner product of the target signal and a sampling pattern,

$$g_k = \boldsymbol{\phi_k}^T \boldsymbol{x}. \tag{1.3}$$

After collecting the K measurements $\boldsymbol{g}$, we wish to determine the target signal $\boldsymbol{x}$ from these measurements and the measurement matrix. Using conventional imaging techniques one would assume that we must measure at or above the Nyquist rate and collect at a rate twice as great as the highest frequency of the target signal. By using knowledge about the sparsity of the target signal, CS may reconstruct a target signal using far fewer measurements $K << N$.

1.2 Motivation and Applications

In a conventional imaging system, each pixel in the final image requires its own detector, typically an element on the focal plane array of the camera. All the data is measured and

then compressed with many of the bits thrown away. Compressive sensing directly acquires data in a compressed domain. This results in fewer bits that must be stored at the sensors location and reduces communication bandwidth requirements. The full resolution data can be reconstructed on demand trading reduced physical sensor, storage and communication costs for increased computational costs.

As commercial high resolution cameras become smaller and cheaper, compressive sensing techniques are less important for the visible EO domain, although the reduced data storage requirements are still of interest. However, these techniques are sorely needed in the Infrared (IR) domain where high resolution FPAs are significantly more expensive with a larger pitch size [1, 2]. With some modifications, CS techniques can also reduce detector costs for photon limited applications including IR and astronomy [3].

Table 1.1 shows how quickly sensor costs go up as the wavelength increases from visible EO to long-wavelength IR (LWIR). In addition to dollar costs, the size and power costs of IR sensors and their required cooling also increase. Space and power are limited for in flight data collection, and reducing weight will also reduce fuel costs. CS techniques can directly reduce all of these costs by using a significantly smaller and cheaper FPA.

Table 1.1: Pixel costs for EO, NIR, SWIR, MWIR, and LWIR sensors

Wavelength	**Detector Technology**	**Approx cost per pixel**
Visible EO (EO)	Silicon (Si)	$< .001¢$
NIR (near-infrared)	Silicon (Si)	$< .001¢$
SWIR (short-wavelength IR)	InGaAs or PbSe	$10¢$
MWIR (mid-wavelength IR)	InSb or PbSe	$10¢$
LWIR (long-wavelength IR)	Bolometer	$1¢$
LWIR (long-wavelength IR)	HgCdTe	$< \$10$

Cost data from [4]

CS techniques are used in other fields beyond conventional image collection. In astronomy [5], large amounts of data is collected with limited on site computing abilities. CS techniques allow for a high compression ratio even if the sparse basis is unknown by the sensor. If measurement patterns are chosen from a library only the pattern indexes and the raw, already compressed data need to be transmitted back to earth. The original data can

be re-constructed off-line reducing on board computing requirements. In the RF regime, dominant backscattered energy generally only results from a small subset of man-made objects in a scene [6]. Thus, radar images from, e.g. a synthetic aperture radar (SAR) system, are generally sparse. Compressive sensing and scene sparsity can be used to reduce the number of radar pulses and enable multi-function radar capabilities [7]. CS also has many applications in the medical field including MRIs [8, 9, 10]. MRIs have a great deal of both temporal and spatial sparsity to exploit allowing CS to significantly reduce the number of measurements required. The goal is to collect fewer measurements without any negative aliasing effects reducing the time patients spend in the machine and increasing the number of patients who can be imaged with one MRI machine.

In this thesis, we focus on image reconstruction in the visible Electro-Optical (EO) domain. AFRL wishes to develop a compressive sensing testbed to explore and evaluate algorithms on real data. We seek to reduce sensor size and cost without reducing image quality. While long-wave applications are of eventual interest, visible EO provided an affordable starting point for rapid development in a laboratory setting.

1.3 The Calibration Problem

In order to successfully reconstruct the target signal $\boldsymbol{x}$ with compressive sensing, the measurement system must be approximately linear, and we must have a good estimate for the measurement matrix $\boldsymbol{\Phi}$. Even when the measurements are designed, as in the case of mirror patterns in a DMD, unknown end-to end system effects impact the effective measurement matrix. Calibration is the process of estimating the measurement matrix from the data. If $\boldsymbol{\Phi}$ is poorly estimated, reconstruction error will increase and more samples will be needed to estimate the target signal accurately. In severe cases reconstruction may be impossible with a poorly calibrated measurement matrix.

The most common [11] calibration approach is to estimate a scalar gain α that applies

to the measurement matrix

$$\boldsymbol{g} = \alpha \boldsymbol{\Phi} \boldsymbol{x}. \tag{1.4}$$

The authors in [12] proposed a calibration procedure that mostly focuses on improving, the testing environment, subtracting background noise, and averaging frames to increase SNR. The Rice Single Pixel Camera (SPC) [13, 14] also subtracted background noise from their measurements by measuring a DC offset when their SLM was set to block all light. This offest was subtracted from their measurements before reconstructing their images. Other systems using a DMD such as [2, 15] focused on the alignment of the mirrors with the detector. The authors in [16] proposed optical solutions to improve results.

1.4 Contributions and Organization

This thesis is structured as follows. Chapter 2 provides a brief mathematical overview of compressive sensing. Section 2.2 contains a more detailed description of the Bayesian compressive sensing framework used in the rest this thesis, and Section 2.3 details the Bayesian CS reconstruction algorithm, fast RVM, used to generate our results.

Our *first major contribution* is presented in Chapter 3, which describes our development of a fully automatic hardware system for a visible EO CS testbed. The testbed included a programmable LED test target and uses a DMD for its Spatial Light Modulator (SLM). The system can automatically collect calibration and testing data for multiple targets.

Our *second major contribution* is presented in Chapter 4 and includes development and estimation methods for new calibration models appropriate for DMD systems. Each model expands on the preceding model, adding in new parameters to those present in the previous model. Model 0 uses no calibration and is presented as a baseline. Model 1

includes a single gain parameter $\boldsymbol{g} = \alpha\boldsymbol{\Phi x}$ as is commonly found in the CS literature. We propose Models 2-4 as original work and compare them to the baseline Model 0 and current state of the art, Model 1. Our *third major contribution* is the release of a public CS dataset produced using our testbed. This is described in Chapter 5, along with results and analyses that demonstrate the improvements achieved when using our new calibration models. In Chapter 6 we summarize our conclusions and present our plans for future research.

Compressive Sensing Reconstruction

2.1 Compressive Sensing

For compressive sensing, a target signal may be represented as a weighted sum of basis vectors,

$$\boldsymbol{x} = \boldsymbol{B}\boldsymbol{w}, \tag{2.1}$$

where $\boldsymbol{B}$ contains a set of basis vectors,

$$\boldsymbol{B} = \underbrace{\begin{bmatrix} \boldsymbol{b}_1 & \boldsymbol{b}_2 & \dots & \boldsymbol{b}_N \end{bmatrix}}_{N \times N}, \tag{2.2}$$

that are chosen to represent $\boldsymbol{x}$ by a sparse vector $\boldsymbol{w}$. Each basis vector $\boldsymbol{b_n}$ has its own associated weight w_n,

$$\boldsymbol{w} = \underbrace{\begin{bmatrix} w_1 \\ w_2 \\ \vdots \\ w_N \end{bmatrix}}_{N \times 1}. \tag{2.3}$$

The CS measurements are generating by applying the measurement matrix $\boldsymbol{\Phi}$ to the signal vector as

$$\boldsymbol{g} = \boldsymbol{\Phi}\boldsymbol{x} = \boldsymbol{\Phi}\boldsymbol{B}\boldsymbol{w} \quad (\boldsymbol{w} \text{ sparse}), \tag{2.4}$$

and wish to recover the sparse weights $\boldsymbol{w}$ from $\boldsymbol{g}$ and $\boldsymbol{\Phi}$. Once the weights are recovered we can form our target signal using (2.1). If the signal $\boldsymbol{x}$ is sparse itself then the the sparsifying basis $\boldsymbol{B}$ is simply the identity matrix yielding $\boldsymbol{w} = \boldsymbol{x}$ and

$$\boldsymbol{g} = \boldsymbol{\Phi}\boldsymbol{x} \quad (\boldsymbol{x} \text{ sparse}). \tag{2.5}$$

Without loss of generality, we assume the later form in this thesis.

It is perhaps nonintuitive why CS can recover a target signal with significantly fewer measurements than the dimensionality of the unknown signal $K << N$. It is important to discuss the conditions under which CS will successfully recover the target signal. [17] offers a comprehensive introduction of these conditions. To briefly summarize, the target signal must be *sparse* i.e. the "information" present in the signal is less than the bandwidth that the signal occupies. In addition, the CS measurements must be *incoherent*, that is they must span the space that the target signal is sampled in. To be incoherent the correlation between the measurement set $\boldsymbol{\Phi}$ and the basis set $\boldsymbol{B}$ must be low.

These two properties gives us some intuitive insight as to how and when CS works. Instead of basing the number of required measurements on N, the dimensionality of the signal, we can base it on the amount of information in the signal measured by the non zero weights of the signal. This holds true as long as the those measurements provide global information about the target scene. In fact, it has been shown that random matrices are highly incoherent with a fixed basis [18]. Examples include i.i.d Gaussian or Bernoulli +/- 1 vectors.

Assuming the signal is truly S-sparse and $\boldsymbol{\Phi}$ and $\boldsymbol{B}$ are maximally incoherent we could perfectly reconstruct the target signal from $S+1$ measurements [14, 17] by searching for the l_0 sparsest weights,

$$\hat{\boldsymbol{w}} = argmin\ ||\boldsymbol{w}||_0 \quad s.t. \quad \boldsymbol{g} = \boldsymbol{\Phi}\boldsymbol{B}^T\boldsymbol{x}, \tag{2.6}$$

but solving this problem is NP hard and is not robust to measurement noise, lack of sparsity, or non maximum incoherence.

Instead, if we sufficiently oversample the signal, we can use an l_1 minimization to find the sparsest weights,

$$\hat{\boldsymbol{w}} = argmin\ ||\boldsymbol{w}||_1 \quad s.t. \quad \boldsymbol{g} = \boldsymbol{\Phi}\boldsymbol{B}^T\boldsymbol{x}. \tag{2.7}$$

This can be solved using linear programming techniques and is referred to as Basis Pursuit. The complexity of these Basis Pursuit techniques is polynomial in N. Additionally, as long as the solution is sufficiently sparse and the measurement matrix is properly designed, the solution is equivalent to the l_0 minimization [19].

Reconstruction time can be further reduced by greedy algorithms, which require an increased oversampling factor. These include the Matching Pursuit family including OMP [20], ROMP [21], StOMP, [22], and others.

2.2 Bayesian Compressive Sensing

Compressive sensing can also be though of in a Bayesian context. We have observed data $\boldsymbol{g}$ and a prior that $\boldsymbol{w}$ should be sparse. We seek a posterior density function that we can use to estimate the sparse weights $\boldsymbol{w}$. This provides not only a value for $\boldsymbol{w}$ which is used to reconstruct the signal but also a measure of uncertainty or "error bars" on each non zero point in the reconstructed signal $\boldsymbol{x}$. We provide an overview of the Bayesian Compressive

Sensing framework introduced by Carin and Tipping and refer the reader to their papers [23, 24, 25] for additional details.

We model our compressive sensing measurements as a weighed sum of random measurements with added noise,

$$\boldsymbol{g} = \boldsymbol{\Phi}\boldsymbol{w} + \boldsymbol{n}. \tag{2.8}$$

The weights, $\boldsymbol{w}$, are adjusted to be sparse and only contain the largest magnitude elements. The noise in Equation (2.8) is modeled from two additive sources. The first comes from the smaller magnitude weights which were removed from $\boldsymbol{w}$. This noise can be approximated as zero-mean Gaussian due to the Central Limit Theorem [26] since the measurement matrix $\boldsymbol{\Phi}$ is composed of random samples. There is measurement noise which can also be modeled as a zero-mean Gaussian distribution. Combining both noise sources allows us to approximate the total system noise as a zero-mean Gaussian with an unknown variance, σ^2, and provides us with a Gaussian likelihood model,

$$p(\boldsymbol{g}|\boldsymbol{w}, \sigma^2) = (2\pi\sigma^2)^{-K/2} \exp\left(\frac{-1}{2\sigma^2}||\boldsymbol{g} - \boldsymbol{\Phi}\boldsymbol{w}||^2\right). \tag{2.9}$$

From here we seek a full posterior density function for $\boldsymbol{w}$ and σ^2.

We wish to define a sparse prior on the weights $\boldsymbol{w}$ which strongly peaks at $w_i = 0$. A commonly used sparse prior is the Laplace density function,

$$p\left(\boldsymbol{w}|\lambda\right) = \left(\frac{\lambda}{2}\right)^N \exp\left(-\lambda \sum_{i=1}^{N} |w_i|\right). \tag{2.10}$$

We want to estimate $\boldsymbol{w}$ using a maximum a posteriori (MAP) estimator [27] which would give us an equivalent solution to l_1 minimization. However, there is no closed form solution using the Laplace prior which is not conjugate to the Gaussian likelihood in Equation (2.9). Instead [23] and [25] derive a hierarchical prior which has similar properties to the Laplace

prior in Equation (2.10). This prior,

$$p\left(\boldsymbol{w}|\boldsymbol{\alpha}\right) = \left(2\pi\right)^{-N/2} \prod_{n=1}^{N} \alpha_n^{1/2} exp\left(-\frac{\alpha_n w_n^2}{2}\right), \tag{2.11}$$

introduces N independent hyperparameters (a parameter that operates on another parameter) $\boldsymbol{\alpha}$. Each element of $\boldsymbol{\alpha}$ controls the strength of the prior for that element's weight, w_n, and α_n is the inverse prior variance, or precision, of w_n [28]. Note that as α_i goes to infinity w_i goes to zero.

If we know $\boldsymbol{\alpha}$, we can use Bayes rule [27] to form a posterior distribution of the weights $\boldsymbol{w}$ from the marginal likelihood in Equation (2.9) and the prior in Equation (2.11)

$$p\left(\boldsymbol{w}|\boldsymbol{g}, \boldsymbol{\alpha}, \sigma^2\right) = p\left(\boldsymbol{g}|\boldsymbol{w}, \sigma^2\right) p\left(\boldsymbol{w}|\boldsymbol{\alpha}\right) p\left(\boldsymbol{g}|\boldsymbol{\alpha}, \sigma^2\right), \tag{2.12}$$

which gives a multivariate Gaussian with the following the following mean and covariance:

$$\boldsymbol{\mu} = \sigma^2 \boldsymbol{\Sigma} \boldsymbol{\Phi}^T \boldsymbol{g}, \tag{2.13}$$

$$\boldsymbol{\Sigma} = \left(\sigma^2 \boldsymbol{\Phi}^T \boldsymbol{\Phi} + \boldsymbol{A}\right)^{-1}, \tag{2.14}$$

where $\boldsymbol{A}$ is a diagonal matrix formed from the hyperparameters, $\boldsymbol{\alpha}$,

$$\boldsymbol{A} = \begin{bmatrix} \alpha_1 & & & \\ & \alpha_2 & & \\ & & \ddots & \\ & & & \alpha_N \end{bmatrix}. \tag{2.15}$$

We use this knowledge to directly estimate the target signal $\boldsymbol{x}$ which is also a multi-

variate Gaussian and has the following mean and covariance:

$$\mathbf{E}(\boldsymbol{x}) = \boldsymbol{B}\boldsymbol{\mu}, \tag{2.16}$$

$$\mathbf{Cov}(\boldsymbol{x}) = \boldsymbol{B}\boldsymbol{\Sigma}\boldsymbol{B}^T. \tag{2.17}$$

Thus, if we can obtain a point measurement for the hyperparmeters $\boldsymbol{\alpha}$ we can reconstruct the target signal from the compressive sensing measurements $\boldsymbol{g}$ and the measurement matrix $\boldsymbol{\Phi}$. This point estimate can be obtained from a type-II maximum likelihood procedure [27] by maximizing the marginal likelihood of $\boldsymbol{\alpha}$.

2.3 Fast RVM

The fast relevance vector machine (RVM) [24, 25] is a BSC reconstruction algorithm that achieves faster run-time and increases sparsity through its ability to dynamically add and delete columns of the measurement matrix, $\boldsymbol{\Phi}$, [23]. We provide a brief overview of the fast RVM algorithm here and refer the reader to [24, 25] for a detailed derivation and [29] for a MATLAB implementation.

Fast RVM initializes with an estimate of σ^2 and a single candidate basis vector ϕ_k. Then, Fast RVM computes a metric that compares s_k, the sparsity of a candidate vector (how much ϕ_k overlaps with the basis vectors currently included in the model) and q_k, the "quality" of the candidate vector (how ϕ_k aligns with the model error when ϕ_k is excluded from the model). This metric is defined as

$$\theta_k = q_i^2 - s_i. \tag{2.18}$$

When this metric is greater than zero, the candidate ϕ_k should be added to the model if currently excluded or the weight α_k should be re-estimated if ϕ_k is already included. When

this metric is less than zero the candidate vector should be deleted from the model. The next candidate vector is chosen by updating values for all vectors and choosing the vector which will maximize the change in marginal likelihood. The candidate vector is added, deleted or, re-estimated based on its sparsity and quality factors. If not known, Fast RVM will provide an updated noise estimate σ^2. Fast RVM terminates when adding or re-estimating any vector would result in a change of the marginal likelihood which is less than the a chosen threshold and there are no other candidates which should be deleted from the model. Fast RVM can also provide a framework for adaptive compressive sensing as discussed in [23].

RVM takes the measurement vector $\boldsymbol{g}$ and its associated measurement matrix $\boldsymbol{\Phi}$ as inputs and outputs the reconstructed signal $\hat{\boldsymbol{x}}$

$$\hat{\boldsymbol{x}} = \text{rvm}(\boldsymbol{g}, \boldsymbol{\Phi}). \tag{2.19}$$

There are two parameters that can be set by the user. The first is a threshold that determines when the algorithm will terminate, lowering this value will increase the run time. We found $thresh = 10^{-6}$ yielded the best results for our data. The second parameter is an initial estimate for σ^2. We used $\sigma^2 = \text{var}(g) \times 0.1$ where $\text{var}(g)$ is the variance of the camera measurements. These are values recommended in [24], although we did test other values to confirm that these were the best choices for our data set.

Acquisition System Development

3.1 System Overview

Our system uses a digital mircromirror device (DMD) to collect compressive sensing measurements. The system is modeled after the setup used by Rice University for their single pixel camera [13]. Figure 3.1 shows the system setup and the four major components of the system.

A simple target is displayed on a LED board. This provides a bright target that can be controlled automatically from a laptop. The target signal is focused on the DMD with a singlet lens. The DMD is an array of small mirrors that are used to spatially modulate the target signal. The spatially modulated signal is captured by the focal plane of a camera with an attached lens which gives us our compressive sensing measurements.

The target, mirror patterns, and camera can all be controlled automatically from a laptop. Each measurement takes approximately 10 seconds to collect. Figure 3.2 shows how the system is connected. A laptop is used to control the camera, DMD, and Raspberry Pi. The Raspberry Pi is used to send the targets to the LED display board. Thin arrows on the flow chart indicate a signal to advance to the next measurement. Thick arrows represent the transfer of data. Curved arrows show how each piece is connected in a cyclical process.

The laptop signals the Raspberry Pi to display the first target. The laptop then sends the first pattern to the DMD. Once the mirrors are set the laptop triggers the camera to take an image. Once the image is saved the next pattern, is displayed on the DMD. After

measurements are taken for all the patterns the next target is displayed and the cycle is repeated until all targets have been imaged.

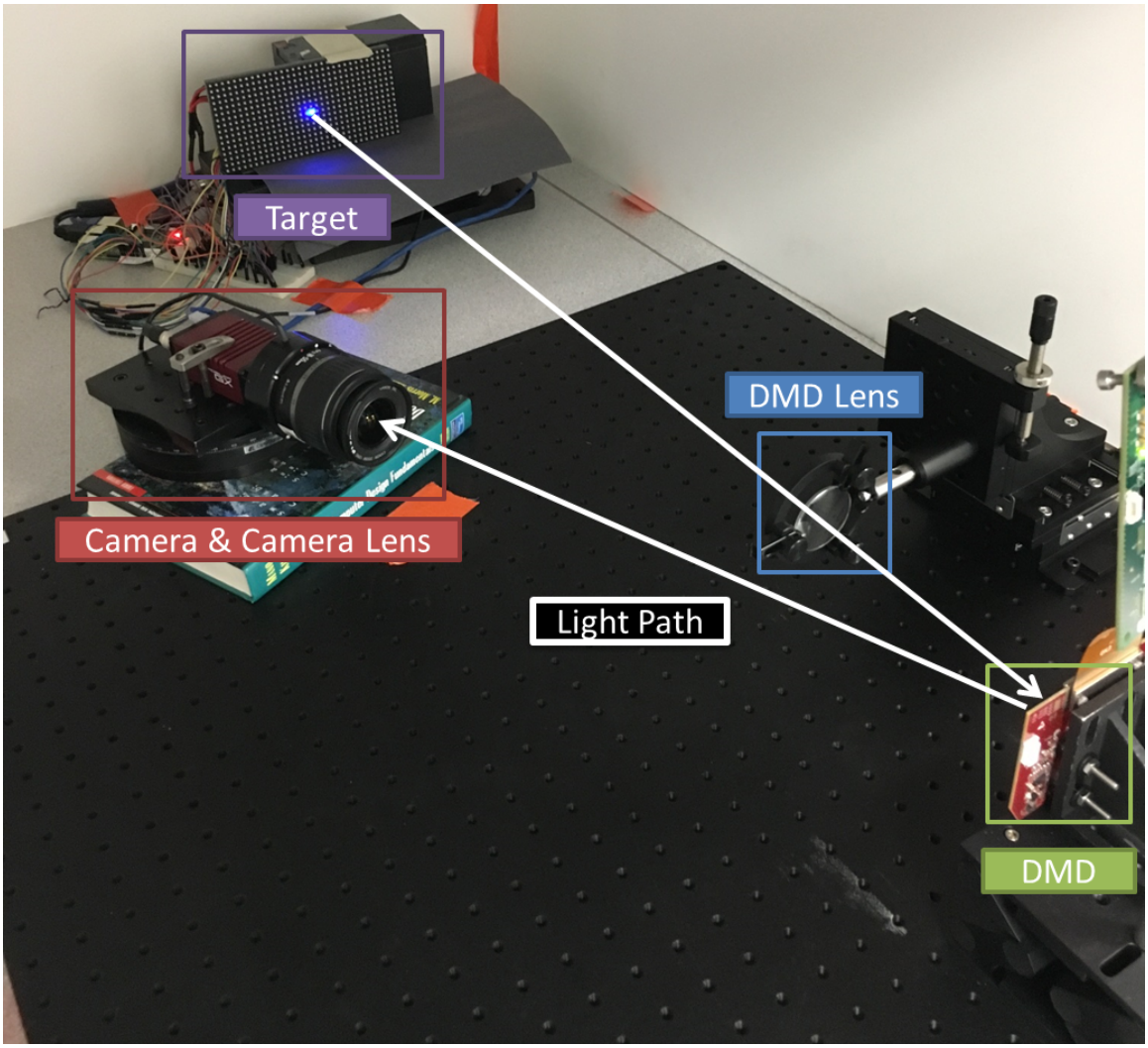

Figure 3.1: System setup

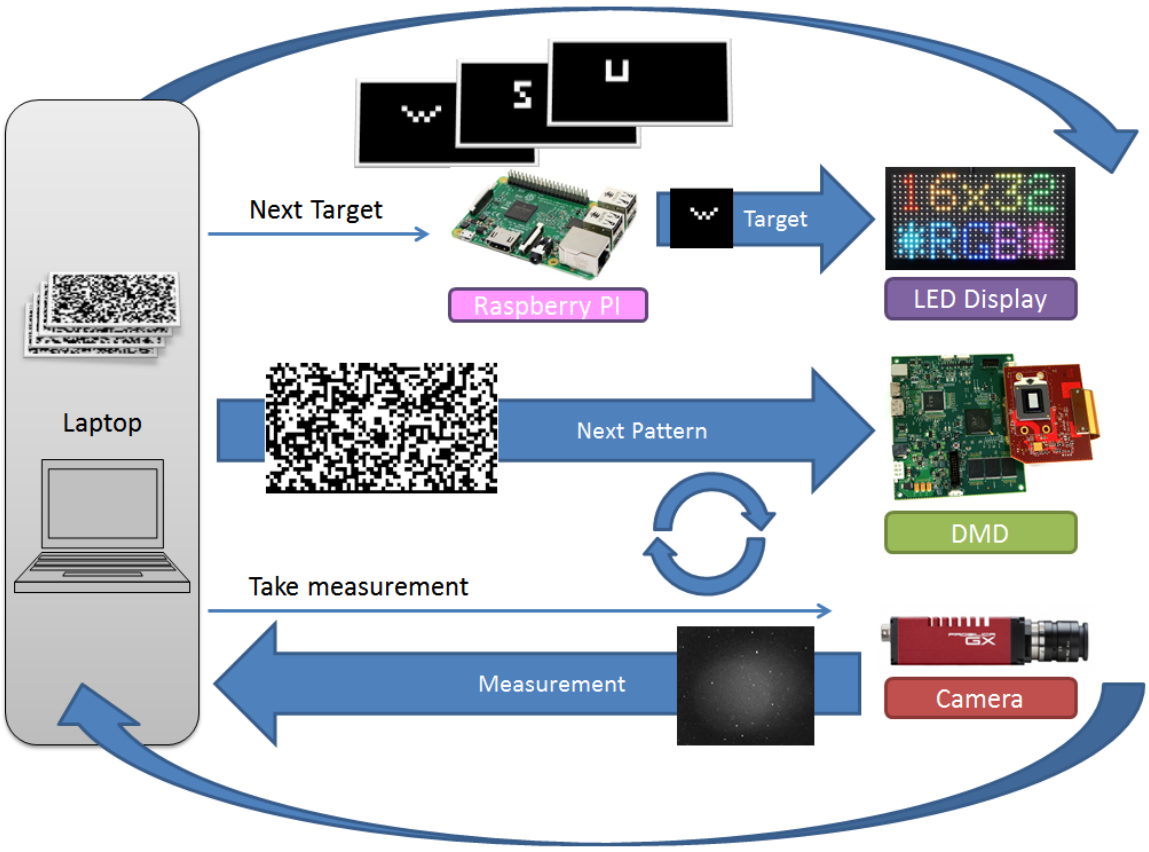

Figure 3.2: System design flowchart

3.2 LED Target Display

The two major design goals for the target were that the target could be changed without disrupting its position in the system and that the target could be changed automatically. We wanted to collect calibration data on a number of different targets and to get good calibration data it was important that the target stayed aligned with the DMD and its lens. This ruled out the paper targets often found in the CS literature since we were not confident that we could change out the target without shifting the alignment. Given the slow time to take a single measurement it was also important that the target was tied into the acquisition system so that it could be changed automatically once the previous target was completed and data collection could continue without waiting for a manual target change.

Our first target was a computer monitor connected to our system laptop that would display the targets as images. This met our design goals for automation and consistency but we found that the signal to noise ratio (SNR) was too low for our application. The main issue was that the contrast was not high enough for our application. We tried to increase the signal by increasing the exposure time on the camera but even a 60 second exposure was not enough.

A Liquid Crystal Display (LCD) monitor contains a series of filters back-light by a florescent light [30]. When pixels are set to black the filters are set to block all light but some of this light will still leak through [31] and black will instead be displayed as a dark gray. For our application we were displaying a mostly black screen with a few pixels set to white. The light introduced by the black pixels weakened our signal enough that we were not able to reconstruct the target.

We changed our target to the 16x32 LED display board [32] shown in Figure 3.3. The LEDs on the board were significantly brighter than a display monitor and the black LEDs were truly off and produced no light. The board could be fixed in place and controlled automatically. This met our design criteria while significantly improving our SNR.

The LED display board has a 16 pin Insulation-Displacement Contact (ICD) connec-

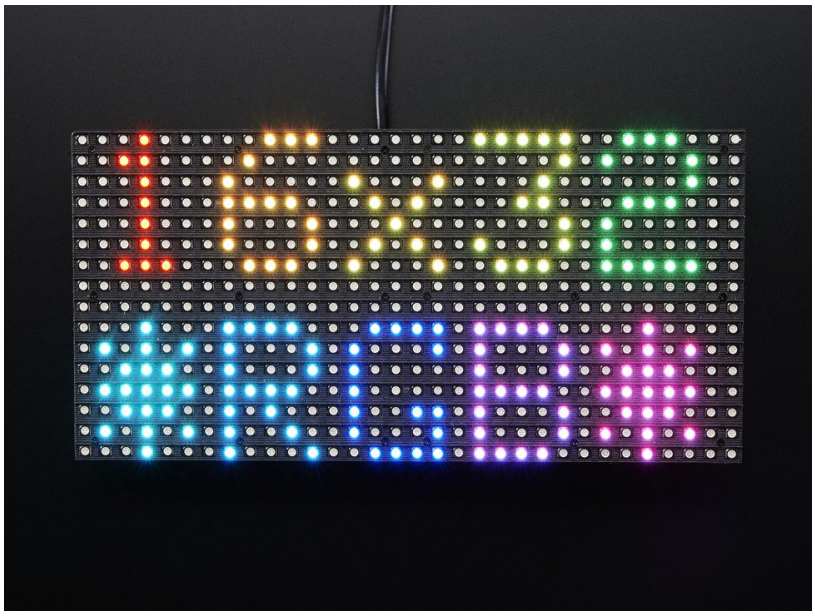

Figure 3.3: 16 x 32 RGB LED display board, image from adafruit [32]

tor that is used to set the LEDs. We can generate the signal to control the LEDs using the General Purpose Input/Output (GPIO) pins on a Raspberry Pi. Using the provided tutorials [33, 34] we connected the two devices through a breadboard. Figure 3.4 shows the completed breadboard setup. We had to use level shifters to shift the 3.3V output from the Raspberry Pi to 5V for the LED board. Reference [34] shows a more permanent wiring solution using a PCB (Printed Circuit Board) but we found the breadboard adequate for our laboratory setup.

Our display board can display multiple colors but we only use white to get the brightest possible target. The targets are stored on the Raspberry Pi as 16x32 images. When the system is ready for a new target the laptop signals the Raspberry Pi via ssh. The Raspberry Pi transmits the signal via the GPIO pins and the target is displayed. Figure 3.5 shows the LED board displaying a calibration target.

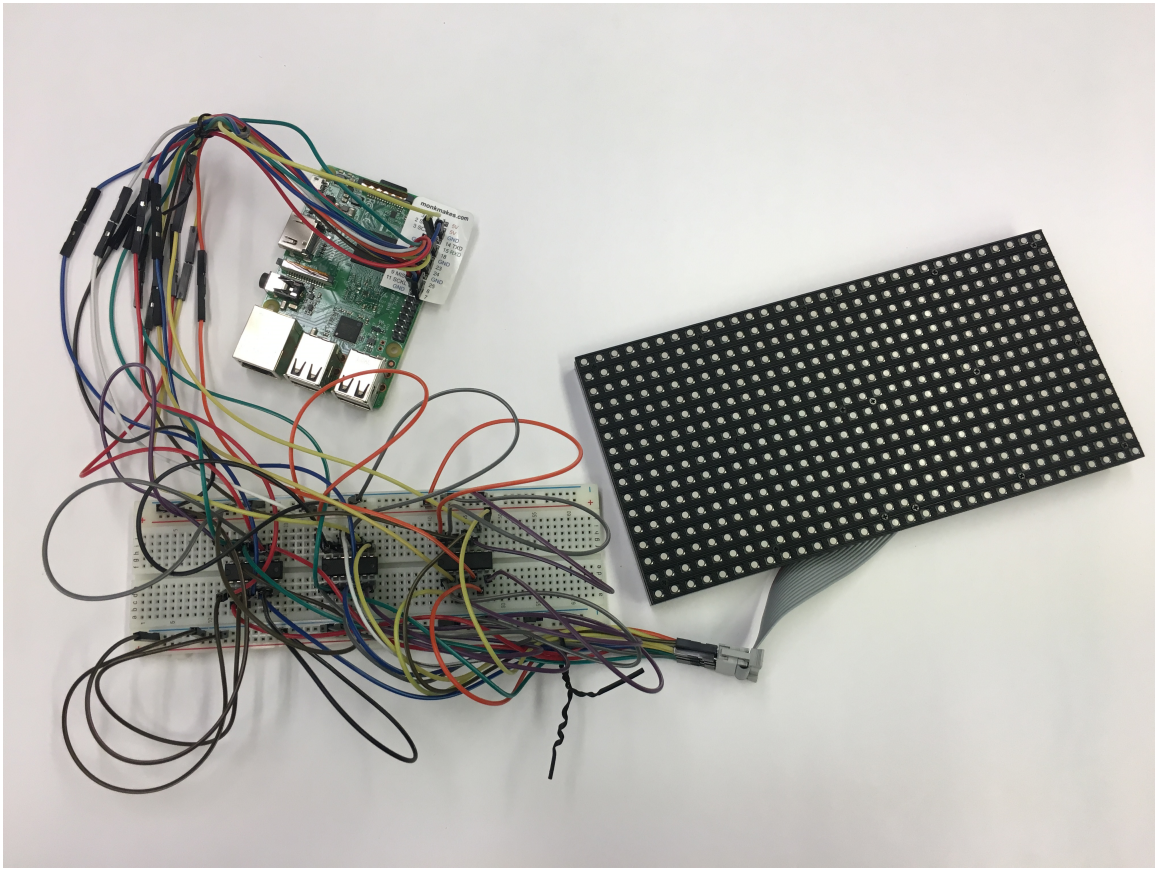

Figure 3.4: Breadboard setup connecting the LED display to the Raspberry Pi

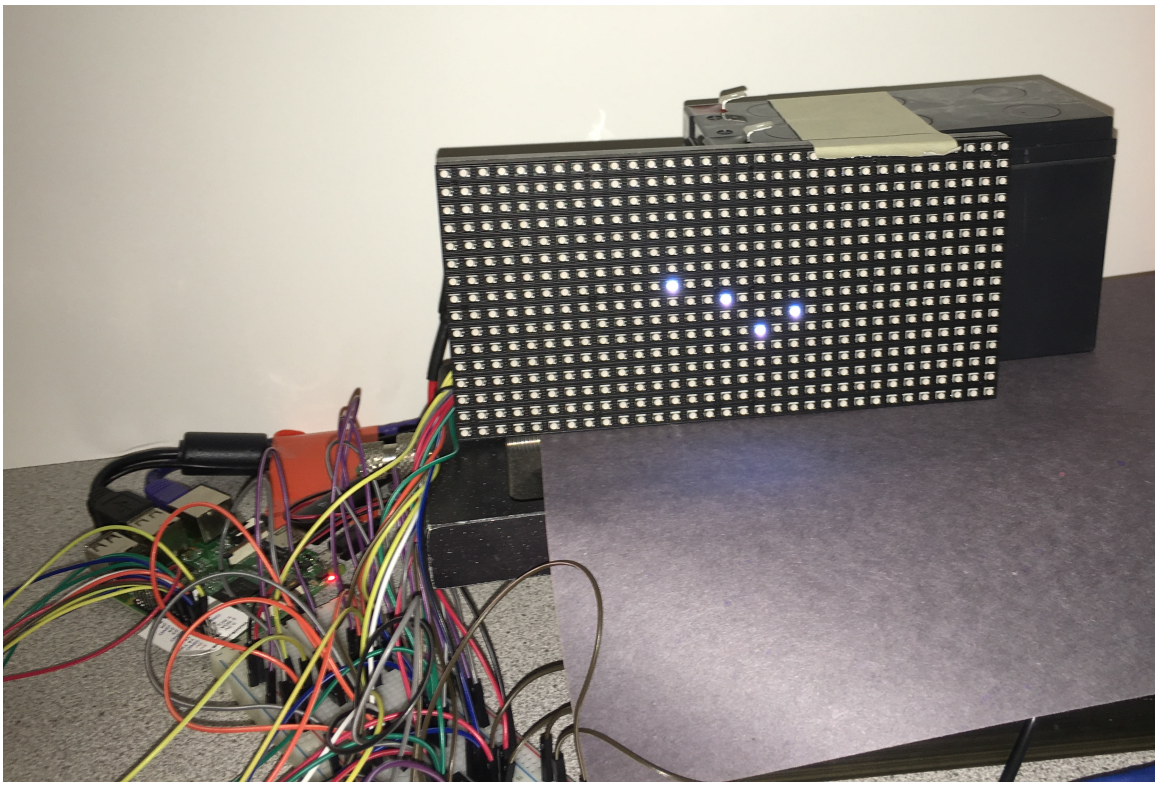

Figure 3.5: LED board displaying a calibration target

3.3 Digital Micromirror Device

A DMD is a two-dimensional array of reflective mircomirrors used to spatially modulate light [35]. Each mirror is controlled individually and can be set to an on or off state. The standard application for DMDs is a projector where the image is displayed on the mirrors and reflected the light is collected into or out of an optical collection aperture [35]. DMDs are used for a number of other applications including 3D scanning, 3D printing and hyperspectral imaging [35]. For compressive sensing the projector application is "reversed" where the incoming light is the target image and only parts of the signal are collected via the on state mirrors. DMDs are a popular choice of spatial light modulators for compressive sensing and have been used in a number of projects including [13, 2, 16].

The mirror array is the physical representation of the measurement matrix Φ in Equation 1.1. The patterns are displayed on the DMD one at a time and a measurement is

taken for each displayed pattern. A pattern is a binary image where the ones represent on -state mirrors and the zeros represent the off -state mirrors. Each binary image pattern is vectorized and stored as a row in Φ.

The DMD mirrors are arranged in two-dimensional grid. When a mirror is turned on, it is tilted at +12 degrees. When a mirror is turned off it is titled at -12 degrees. The light reflected at +12 degrees is collected on the focal plane of the camera to obtain the measurement. Figure 3.6 shows the operation of the micro mirrors. The exact angle of the mirror tilt will depend on the DMD model and manufacturer.

We used a TI Light Crafter 6500 Evaluation Model [35] for our DMD. The DMD was chosen since it included software to control the mirror patterns [36]. The Light Crafter 6500 is shown in Figure 3.7 with the mirror array highlighted. Figure 3.8 shows the DMD installed in our system. The physical dimensions of the mirror array are 14.5 mm x 8.1 mm. The mirror array contains 1920x1080 mirco mirrors. The pattern rate for 1-bit images is 9500 Hz although for our application it is much slower.

The included Light Crafter software is used to control the mirror patterns. The DMD package contains some on-board memory but only 400 unique images can be stored at a time. Since more measurements than this are required the pattern images are stored on a laptop, and uploaded one at a time. This upload time is the slowest part of the data collection process with a single 1920x1080 mirror pattern taking over a minute to upload. To reduce both upload time and the number of measurements needed, we address the mirror in 32x32 "super mirror" blocks, where all mircomirros within the block are always assigned the same on or off state. This reduces the pattern size to 60x34 and allows us to upload a pattern in under one second. For the rest of this thesis when we refer to a single mirror we mean a 32x32 super mirror block unless otherwise specified.

Figure 3.9 shows the difference between a full 1920x1080 mirror pattern and a 60x34 super mirror pattern. Note that the size reduction results in an unused partial row of super mirrors at the bottom of each pattern image. Each uploaded pattern is still 1920x1080 with

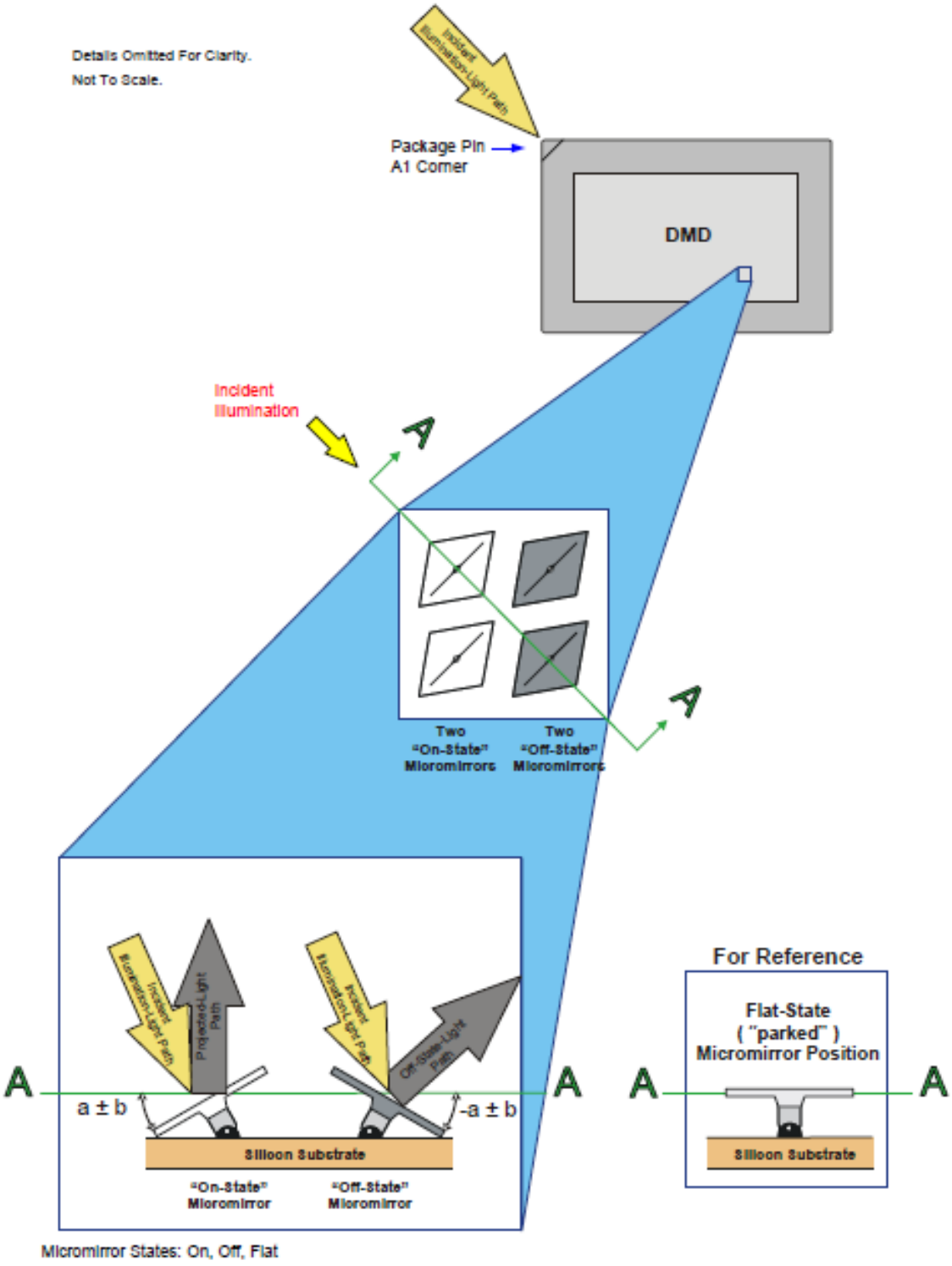

Figure 3.6: DMD mirror operation, image from TI data sheet [35]

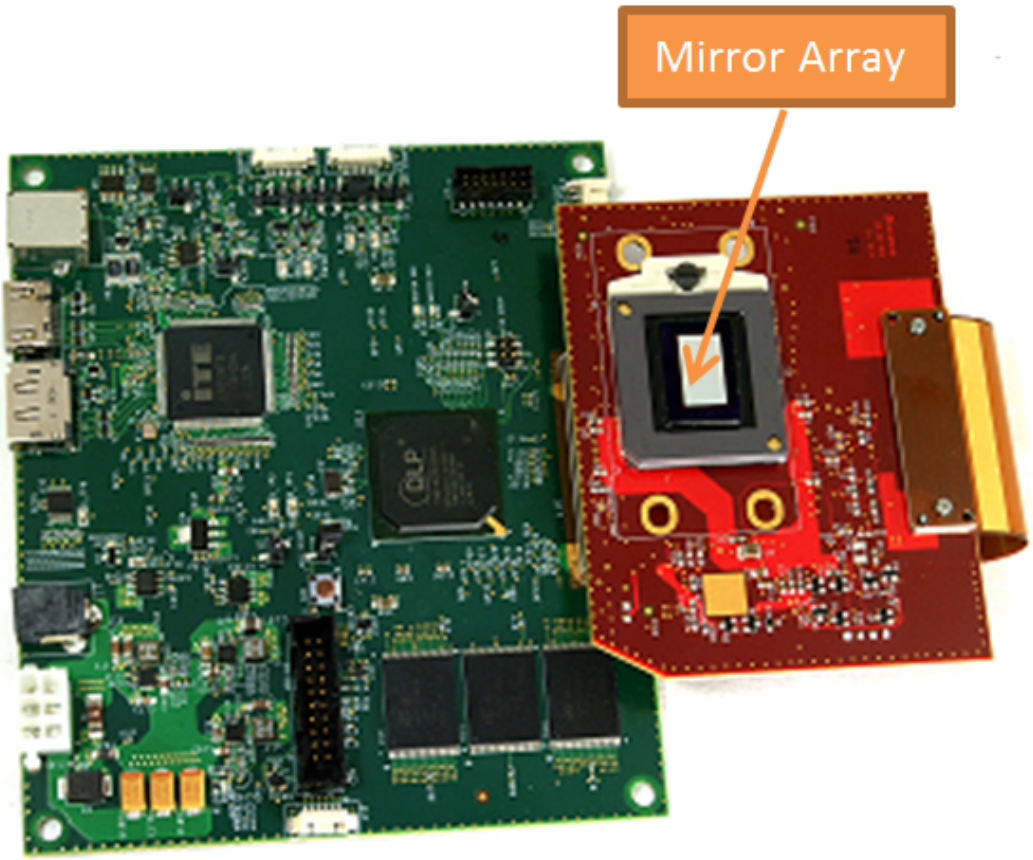

Figure 3.7: TI Light Crafter 6500 DMD, image from TI data sheet [35]

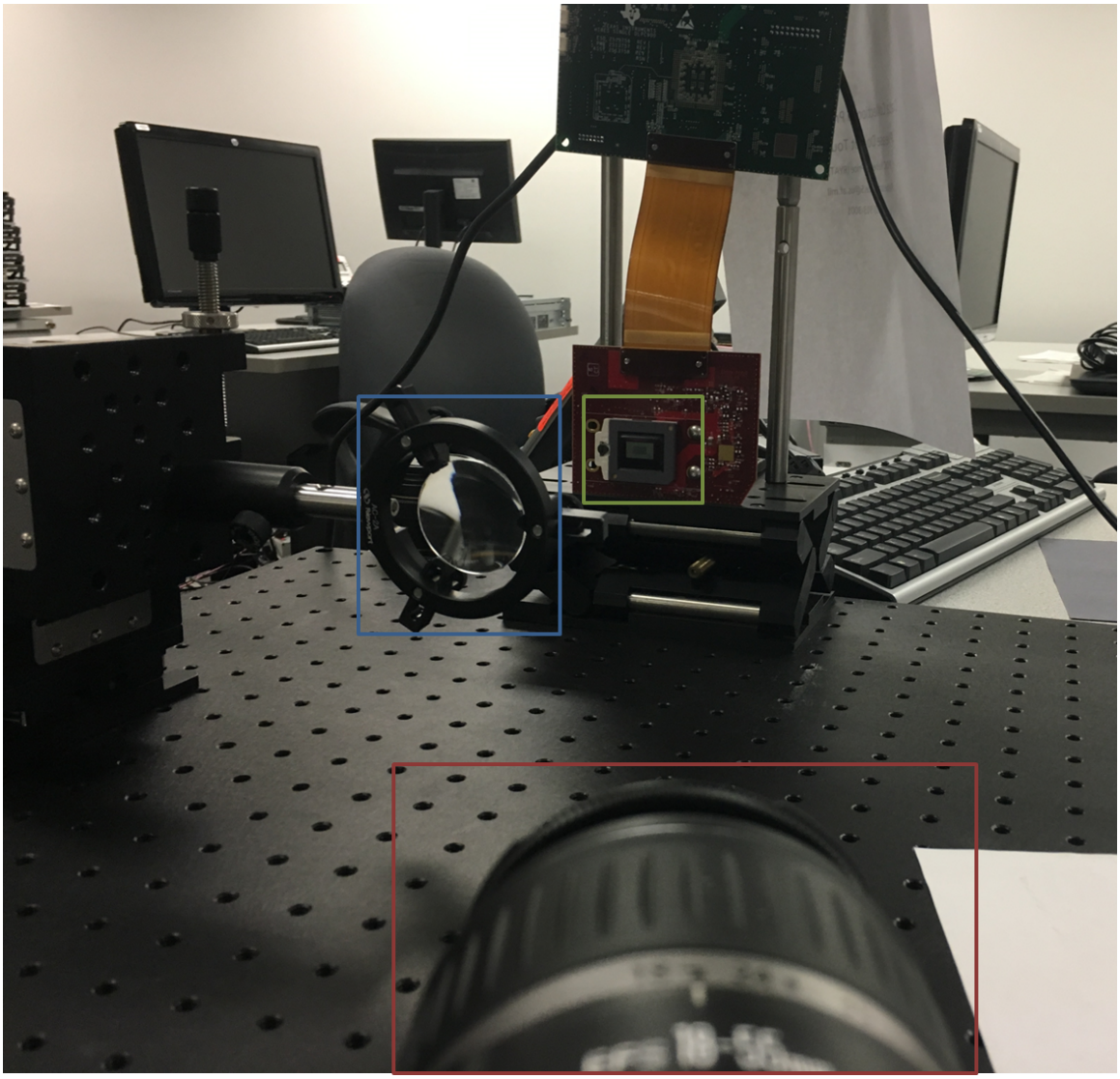

Figure 3.8: Light Crafter 6500 DMD installed in the system

these extra mirrors left turned off. A 60x34 pattern is still used for reconstruction.

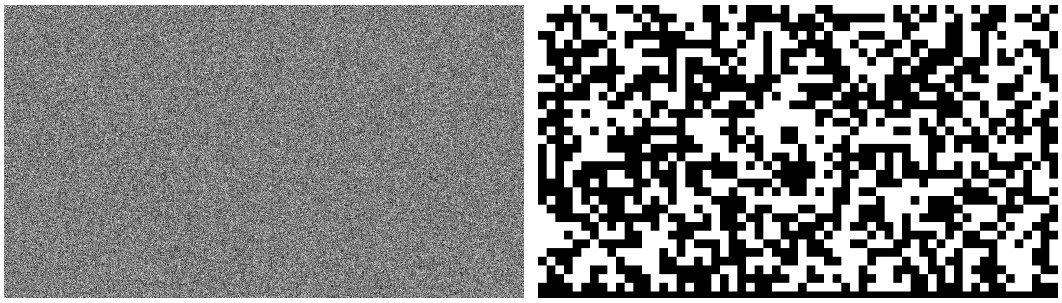

(a) Full 1920x1080 random pattern

(b) 60x34 random pattern addressed by 32x32 super mirrors

Figure 3.9: Patterns comprised of super mirrors compared to individual mirrors

In this thesis, we use random Bernoulli patterns comprised of only ones and zeros. However, DMDs have been used to form more complex patterns for CS. The mirrors could be duty cycled to increase the number of possible values [14]. The authors in [2] generated +/- 1 Bernoulli patterns by subtracting measurements of two complementary patterns for each CS measurements and saw improved reconstruction performance. Hadamard patterns were used by [16] in place of random Bernoulli patterns which also led to improved reconstruction results. The DMD could also be used to "zoom in" on a region of interest or uncertainty by adaptively adjusting the size of the supermirrors [14].

The DMD was the largest source of measurement noise for our system. The mirror angles are not exact and may drift away from +/- 12 degrees. The off state mirrors can also pick up some light that does not come from the target. There was some light pollution in our testing environment. Additionally, the on state mirrors do not reflect all of the incoming light and the off state mirrors did not block all of the incoming light. Optical aberrations are also introduced when the DMD is not perfectly aligned and on axis with the other components in the system. A number of these noise sources can be reduced by calibration as discussed in Chapter 4. Figure 3.10 shows the effect of the noise introduced by the DMD. In the right image, the DMD is blocked by a sheet of paper. This shows the incoming light unaffected by the mirrors. In the left image, the all mirrors are turned on

with the same target signal.

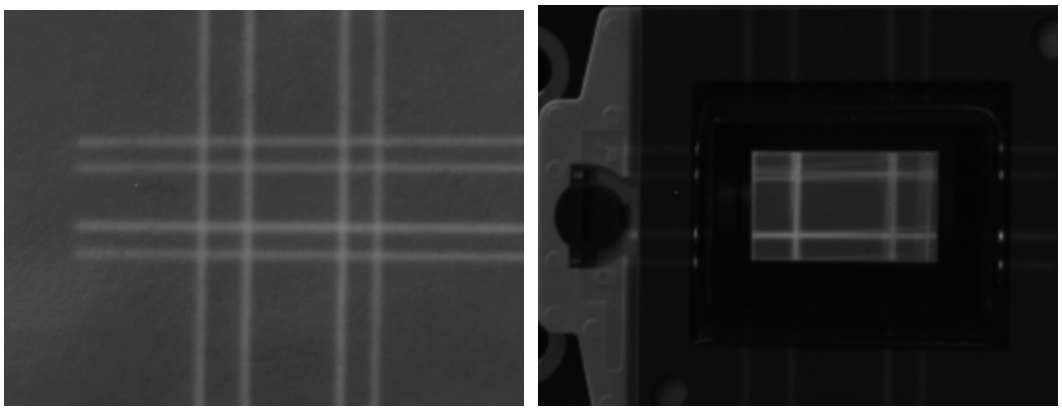

(a) Input: incoming light to the DMD (b) Output: light reflected off the DMD

Figure 3.10: A qualitative assessment of DMD noise seen by comparing incoming and outgoing light from the DMD

3.4 Optical Design

The choice of optical components can have a large effect on CS reconstruction performance. This thesis focuses on improving CS reconstruction through calibration instead of optical improvements. We will briefly discuss some optical concerns here and direct an interested reader to [37] as in introduction to optical design and [15, 16] for a more rigorous analysis of optical concerns for compressive sensing.

Our light path is shown in Figure 3.1. We needed to choose a lens to focus the target light on to the DMD, and a lens to focus the reflected light on the focal plane of the camera. Fixed parameters were the size of the DMD, the size of the FPA, and the 24 degree angle between on and off state reflected light. We could chose the focal length of our lenses and the distance between the different components. Of concern to us is the back focal length of the lens, which determines how close we can place our lens to the DMD and still form an image. Remember that the on light is reflected from the DMD at 24 degrees and cannot pass through the DMD lens again. We needed to fit our testbed on a six foot table due to

space constraints in our laboratory.

We had a 200 mm focal length singlet lens available. We found that placing the lens approximately 8 inches away from the DMD allowed us to focus the LED target placed at the end of our table approximately 50 inches away. The mirror array could see 5 rows of LEDs. Ideally we wanted to focus the light reflected from the DMD onto a single element of the FPA. However, this was not possible using standard optics and the table space available to us. We would need a magnification factor of 6.77×10^{-4} to focus our object, the 8 mm high [35] image formed on the DMD, onto the 5.5 μm high [38] cell of the FPA. We chose a short 18mm lens for our camera to reduce the area of the FPA used. The next section describes how we simulated a single-pixel camera with using this optical setup.

3.5 Data Collection

The camera is used to collect the compressive sensing measurements. The camera captures the spatially modulated light reflected from the DMD and saves it as an image. We used a Prosilica GX 1050 [38, 39] which was chosen due to its accurate trigger mechanism. While we controlled and triggered all components via software, we could have chosen to control both the camera and DMD via a hardware trigger. We were also able to control the exposure and aperture for the camera [39].

The target is a 16x32 image such as in 3.11(a). The LEDs corresponding to the white pixels are turned on and that light is focused on to the DMD. A random 60x34 mirror pattern such as 3.11(b) is displayed on the DMD in order to spatially modulate the light. This light is collected by the camera lens and focused onto the focal plane array of the camera. Ideally, we would like to see this light focused onto a single pixel of the camera. However, due to the optical constraints discussed in Section 3.4 the light hits a larger region of the focal plane array. In this work, we simulate a single pixel camera by de-focusing the camera lens and spreading the light out on to a known region of the focal plane. We can then crop out a

smaller 153x133 image containing that region from the 1024x1024 image collected by the camera giving us an image such as 3.11(c). By averaging the inner 153x133 elements, we acquire a single-pixel measurement representing an integration over all mirror elements of the DMD. We sample the target with K patterns and store these single measurements in a $K \times 1$ data vector $\boldsymbol{g}$. Figure 3.12 shows an example data vector. Image reconstruction is performed directly from this data vector. No other information from the camera is used.

(a) W target (b) DMD pattern (c) Camera measurement

Figure 3.11: Capturing a measurement

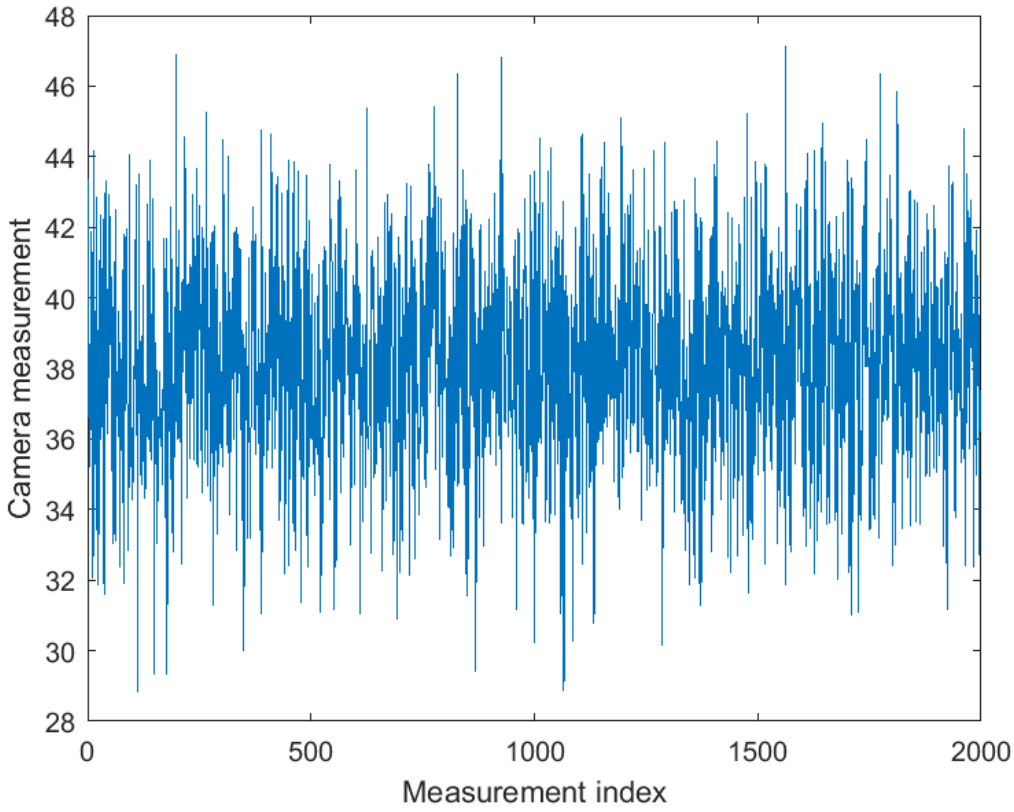

Figure 3.12: Measurement vector $\boldsymbol{g}$

Calibration

4.1 Introduction

We now reintroduce our basic compressive sensing equation

$$\boldsymbol{g} = \boldsymbol{\Phi}\boldsymbol{x} + \boldsymbol{n} \tag{4.1}$$

where a noisy measurement vector $\boldsymbol{g}$ is formed from a measurement matrix $\boldsymbol{\Phi}$ and a target signal $\boldsymbol{x}$. Our DMD mirror states inform the structure of the measurement matrix $\boldsymbol{\Phi}$. Standard compressive sensing literature using a DMD assumes that the measurement matrix $\boldsymbol{\Phi}$ can be modeled by a matrix of ones and zeros corresponding to the on and off mirrors, respectively. We propose that we can improve reconstruction results by applying more sophisticated models for the measurement matrix $\boldsymbol{\Phi}$ based on the mirror state patterns $\boldsymbol{P}$ and additional end-to-end system effects, captured by a parameter vector $\boldsymbol{\theta}$. In this section, we develop four different models for $\boldsymbol{\Phi}(\boldsymbol{\theta})$ that span a range of model complexities. All of the models are inspired by measurements made using our measurement system described in Section 5.1.

The parameters $\boldsymbol{\theta}$ for each calibration model are estimated using a known calibration target and CS measurement pair $(\boldsymbol{x}, \boldsymbol{g})$. The estimated parameters $\hat{\boldsymbol{\theta}}$ are then used to

produce a measurement matrix estimate,

$$\hat{\mathbf{\Phi}} = \mathbf{\Phi}(\hat{\boldsymbol{\theta}}), \tag{4.2}$$

for use in subsequent reconstruction of new test targets, $\boldsymbol{g}_{test} = \hat{\mathbf{\Phi}}\boldsymbol{x}_{test} + \boldsymbol{n}$. The models are initially presented assuming a single target-measurement pair $(\boldsymbol{x}, \boldsymbol{g})$. In Section 4.7, we extend these results to include multiple target-measurement pairs to exploit the availability of multiple calibration targets.

Notation: The measurement vector $\boldsymbol{g}$ contains K measurements, each corresponding to a different pattern of the DMD, which is an $m \times n$ array. For mathematical convenience, we represent the kth pattern as an $mn \times 1$ vector $\boldsymbol{p}_k$ of ones and zeros, representing on- and off-state mirrors, respectively. The target image is also vectorized as $\boldsymbol{x}$ such that $\boldsymbol{p}_k^T\boldsymbol{x}$ represents the inner product between the kth pattern and the target image. The number of elements in $\boldsymbol{p}_k$ and $\boldsymbol{x}$ is represented by $N = mn$. It is occasionally convenient to depict the mirror patterns as an $m \times n$ image as they physically appear on the DMD. To "un-vectorize" a pattern we use brackets as an operator on the enclosed vector, for example

$$[p_k] = \tag{4.3}$$

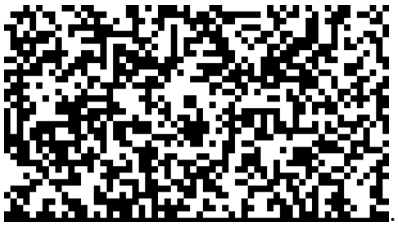

The collection of DMD patterns $\boldsymbol{p}_1, \ldots, \boldsymbol{p}_K$ are stacked as

$$\boldsymbol{P} = \underbrace{\begin{bmatrix} \boldsymbol{p}_1^T \\ \boldsymbol{p}_2^T \\ \vdots \\ \boldsymbol{p}_K^T \end{bmatrix}}_{K \times N}. \tag{4.4}$$

Similarly, the measurement matrix $\boldsymbol{\Phi}$ is viewed as a concatenation of $\boldsymbol{\phi}_k$ operators

$$\boldsymbol{\Phi} = \underbrace{\begin{bmatrix} \boldsymbol{\phi}_\mathbf{1}^T \\ \boldsymbol{\phi}_\mathbf{2}^T \\ \vdots \\ \boldsymbol{\phi}_\boldsymbol{K}^T \end{bmatrix}}_{K \times N} \tag{4.5}$$

such that the kth measurement, $g_k = \boldsymbol{\phi}_k^T \boldsymbol{x}$, is the kth element of the measurement vector $\boldsymbol{g} = \boldsymbol{\Phi}\boldsymbol{x}$. As with the raw patterns, the kth operator may be depicted in un-vectorized form as $[\boldsymbol{\phi}_k]$.

4.2 Model 0: Baseline

Model 0 represents a baseline model that has no calibration. We make the assumption that the measurement matrix $\boldsymbol{\Phi}$ can be modeled with only zeros and ones representing the mirrors on the DMD, i.e.,

$$\boldsymbol{\Phi} = \boldsymbol{P}. \tag{4.6}$$

As the model assumes that the measurement vector $\boldsymbol{g}$ contains direct reflections from the target, there are no parameters or optimization required for this model. Recalling the

RVM syntax of Section 2.3, the estimate $\hat{\boldsymbol{x}}$ of an image $\boldsymbol{x}$ is simply

$$\hat{\boldsymbol{x}} = \text{rvm}(\boldsymbol{g}, \boldsymbol{P}). \tag{4.7}$$

While this basic approach has worked for a number or other systems, we found that calibration improved reconstruction performance and reduced the number of samples required.

4.3 Model 1: Scalar Gain

We start with a single-gain model, commonly found in compressive sensing literature [11]. Model 1 introduces a single calibration parameter α which acts as a gain on the on state mirrors allowing those mirrors to be modeled with any constant. We model our measurement matrix as

$$\boldsymbol{\Phi} = \alpha \boldsymbol{P} \tag{4.8}$$

which will apply the α gain parameter to each on mirror.

As a running example, we introduce a specific 3×3 DMD mirror pattern

$$[\boldsymbol{p}_k] = \begin{bmatrix} 0 & 1 & 1 \\ 1 & 0 & 0 \\ 1 & 0 & 1 \end{bmatrix}, \tag{4.9}$$

which we will use to demonstrate the resulting measurement matrix proposed by each of the models. Using the model in Equation (4.8) we generate this calibrated pattern from the

measurement matrix,

$$[\boldsymbol{\phi}_k] = \begin{bmatrix} 0 & \alpha & \alpha \\ \alpha & 0 & 0 \\ \alpha & 0 & \alpha \end{bmatrix}, \tag{4.10}$$

where the on mirrors are represented with α instead of a one.

We use the measurement matrix to construct the system model,

$$\boldsymbol{g} = \underbrace{\alpha \boldsymbol{P}}_{\boldsymbol{\Phi}(\alpha)} \boldsymbol{x} + \boldsymbol{n}, \tag{4.11}$$

however unlike *reconstruction* where $\boldsymbol{g}$ and $\boldsymbol{\Phi}$ are known and we estimate $\boldsymbol{x}$, in *calibration* $\boldsymbol{g}$ and $\boldsymbol{x}$ are known and we estimate $\boldsymbol{\Phi}(\alpha)$, which for Model 1 means estimation of α. Letting $\boldsymbol{s} = \boldsymbol{\Phi}(\alpha)\boldsymbol{x}$ be the modeled noiseless signal, we may estimate α in the least-squares sense by minimizing the difference between the modeled and actual measurements. That is, we seek $\hat{\alpha} = \arg\min J(\alpha)$ that minimizes the cost

$$J(\alpha) = \sum_{k=1}^{K} (g_k - s_k)^2 \tag{4.12}$$

$$= (\boldsymbol{g} - \alpha \boldsymbol{P}\boldsymbol{x})^T (\boldsymbol{g} - \alpha \boldsymbol{P}\boldsymbol{x}). \tag{4.13}$$

The cost is quadratic and therefore has a unique minimum. Expanding $J(\alpha)$ and equating the derivative to zero, we have

$$J(\alpha) = \boldsymbol{g}^T\boldsymbol{g} - 2\alpha \boldsymbol{g}^T \boldsymbol{P}\boldsymbol{x} + \alpha^2 \boldsymbol{x}^T \boldsymbol{P}^T \boldsymbol{P}\boldsymbol{x} \tag{4.14}$$

$$\frac{\mathrm{d}J(\alpha)}{\mathrm{d}\alpha} = -2\boldsymbol{g}^T \boldsymbol{P}\boldsymbol{x} + 2\alpha \boldsymbol{x}^T \boldsymbol{P}^T \boldsymbol{P}\boldsymbol{x} = 0. \tag{4.15}$$

Solving for α, we obtain the scalar gain estimate

$$\hat{\alpha} = \frac{\boldsymbol{g}^T \boldsymbol{P} \boldsymbol{x}}{\boldsymbol{x}^T \boldsymbol{P}^T \boldsymbol{P} \boldsymbol{x}} \tag{4.16}$$

$$= \frac{\sum_{k=1}^{K} (g_k {\boldsymbol{p}_k}^T \boldsymbol{x})}{\sum_{k=1}^{K} ({\boldsymbol{p}_k}^T \boldsymbol{x})^2}. \tag{4.17}$$

Using $\hat{\alpha}$, the estimated measurement matrix is $\hat{\Phi} = \boldsymbol{\Phi}(\hat{\alpha})$ which can be used in subsequent reconstructions to estimate test targets $\boldsymbol{x}_{test}$ from test data $\boldsymbol{g}_{test}$ as

$$\hat{\boldsymbol{x}}_{test} = \text{rvm}(\boldsymbol{g}_{test}, \hat{\boldsymbol{\Phi}}). \tag{4.18}$$

This simple model only accounts for a small number of issues introduced by the measurement system and DMD as the single parameter α can only affect the on state mirrors. We observed that the off state mirrors were a major noise source for our system as discussed in the next section.

4.4 Model 2: On- and Off-State Gains

While the single-gain model described in Section 4.3 is prevalent in the compressive sensing literature, our experiments with optical targets and our micromirror array revealed that non-negligible energy was still reflected by mirrors in the off state. Figure 4.1 illustrates the results of an experiment designed to demonstrate this effect. In the experiment, the camera was focused when this image was taken to more clearly show the observed effect. In this image 32 LED target lights were turned on and the majority of the micromirrors were set to off . One micromirror was turned on and the target light reflected from it can be seen as the bright spot near the middle of the image. However, the 31 LED targets can also still be clearly seen. The previous models assume that no light be reflected from off mirrors which is clearly not the case.

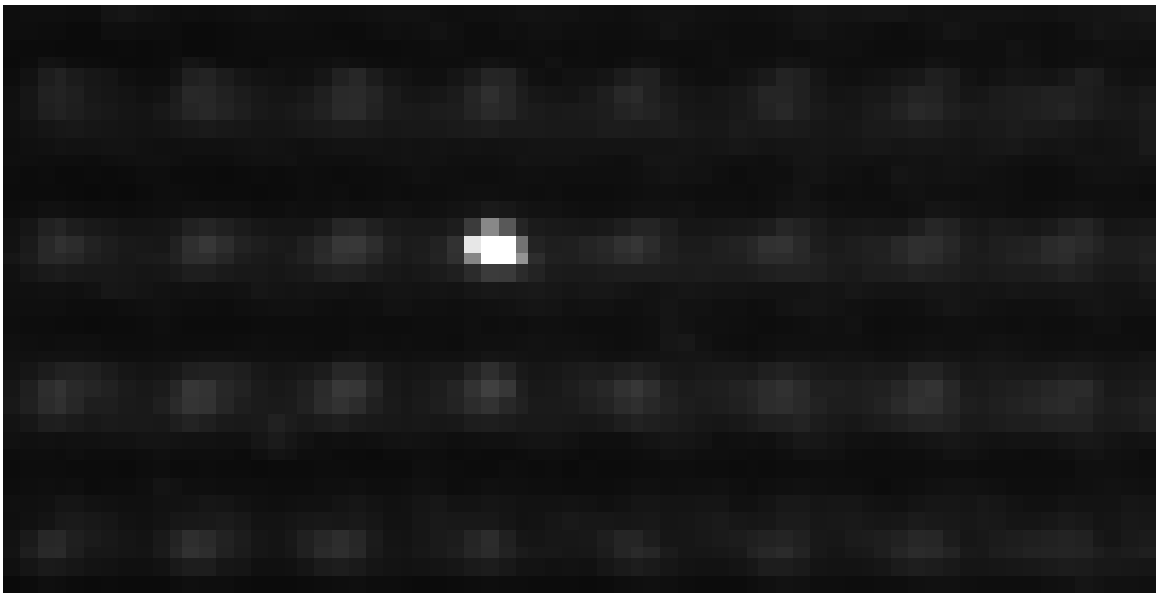

Figure 4.1: Mirrors still reflect light, even when set in the off state.

To model this behavior, we augmented Model 1 by adding in a second gain parameter. Now, a gain α_1 applies to on state mirrors as it did in Model 1. A new parameter α_0 applies to off state mirrors. Adding in this second parameters allows us to account for the off mirrors still reflecting light and model how much light is being reflected. In order to effect separate gains to the different mirror states, we apply α_1 to the on-state mirror elements via $\boldsymbol{P}$, and we apply α_0 to the off-state mirror elements using the complement of $\boldsymbol{P}$, denoted $\boldsymbol{P}^C$. The resulting measurement matrix for Model 2 is

$$\boldsymbol{\Phi} = \alpha_1 \boldsymbol{P} + \alpha_0 \boldsymbol{P}^C. \tag{4.19}$$

This lets us build a measurement matrix that reflects different amounts of light for each mirror state. Recalling the sample mirror pattern $[p_k]$ from Equation (4.9), the complement is

$$[\boldsymbol{p}_k]^C = \begin{bmatrix} 1 & 0 & 0 \\ 0 & 1 & 1 \\ 0 & 1 & 0 \end{bmatrix}, \tag{4.20}$$

and by applying the model in (4.19) we build the measurement matrix which uses both gain terms

$$[\boldsymbol{\phi}_k] = \begin{bmatrix} \alpha_0 & \alpha_1 & \alpha_1 \\ \alpha_1 & \alpha_0 & \alpha_0 \\ \alpha_1 & \alpha_0 & \alpha_1 \end{bmatrix}. \tag{4.21}$$

To find the calibration parameters, we insert (4.19) into the forward model

$$\boldsymbol{g} = \underbrace{\left(\alpha_1 \boldsymbol{P} + \alpha_0 \boldsymbol{P}^C\right)}_{\boldsymbol{\Phi}} \boldsymbol{x}, \tag{4.22}$$

which is rearranged to explicitly indicate the linear dependence on the unknown gain parameters

$$\boldsymbol{g} = \underbrace{\begin{bmatrix} \boldsymbol{P}\boldsymbol{x} & \boldsymbol{P}^C\boldsymbol{x} \end{bmatrix}}_{\boldsymbol{Q}} \underbrace{\begin{bmatrix} \alpha_1 \\ \alpha_0 \end{bmatrix}}_{\boldsymbol{\theta}}. \tag{4.23}$$

With $\boldsymbol{g}$ and $\boldsymbol{x}$ (and therefore $\boldsymbol{Q}$) known, the least-squares estimate of the parameter vector $\boldsymbol{\theta}$ is given in closed-form [27] as

$$\hat{\boldsymbol{\theta}} = (\boldsymbol{Q}^T\boldsymbol{Q})^{-1}\boldsymbol{Q}^T\boldsymbol{g}. \tag{4.24}$$

The estimated parameters $\hat{\alpha}_0$ and $\hat{\alpha}_1$ are used to form the calibrated measurement matrix,

$$\hat{\boldsymbol{\Phi}} = \boldsymbol{\Phi}(\hat{\boldsymbol{\theta}}) = \hat{\alpha}_1 \boldsymbol{P} + \hat{\alpha}_0 \boldsymbol{P}^C, \tag{4.25}$$

and a test signal $\boldsymbol{g}_{test}$ can be used to reconstruct a target $\boldsymbol{x}_{test}$ as

$$\hat{\boldsymbol{x}}_{test} = \text{rvm}(\boldsymbol{g}_{test}, \hat{\boldsymbol{\Phi}}). \tag{4.26}$$

Results in Chapter 5 demonstrate that the increased fidelity of Model 2 significantly im-

proves reconstrutcion performance.

4.5 Model 3: On- and Off-state Gains with Bias

It was further observed that ambient (non-target) illumination sources, and potentially DC offsets in the sensor, lead to target-independent biases in the measurements. To capture these effects, we introduce Model 3, which builds upon Model 2 by adding in a DC offset to the light reflected from the mirrors in each state. Let x_i be a given pixel, and let y_i denote the light reflected from the cooresponding mirror, then in order to capture non-target biases we adopt the following model

$$y_i = \begin{cases} \alpha_0 x_i + \beta_0, & \text{mirror off} \\ \alpha_1 x_i + \beta_1, & \text{mirror on} \end{cases}. \tag{4.27}$$

The gains α_0 and α_1 are as described in Calibration Model 2, while β_0 and β_1 are newly introduced state-dependent DC offsets that do not depend on the target signal. Using (4.27), the measurement system takes the form

$$\boldsymbol{g} = \left(\alpha_1 \boldsymbol{P} + \alpha_0 \boldsymbol{P}^C\right) \boldsymbol{x} + \left(\beta_1 \boldsymbol{P} + \beta_0 \boldsymbol{P}^C\right) \mathbf{1} \tag{4.28}$$

where $\mathbf{1}$ is a $N \times 1$ vector of ones. With a calibration target $\boldsymbol{x}$ know, the measurements may be rearranged into a system that in linear in the unknown calibration parameters $\tilde{\boldsymbol{\theta}}$

$$\boldsymbol{g} = \underbrace{\begin{bmatrix} \boldsymbol{P}\boldsymbol{x} & \boldsymbol{P}^C\boldsymbol{x} & \boldsymbol{P}\mathbf{1} & \boldsymbol{P}^C\mathbf{1} \end{bmatrix}}_{\tilde{\boldsymbol{Q}}} \underbrace{\begin{bmatrix} \alpha_1 \\ \alpha_0 \\ \beta_1 \\ \beta_0 \end{bmatrix}}_{\tilde{\boldsymbol{\theta}}}. \tag{4.29}$$

However, the system $\boldsymbol{g} = \tilde{\boldsymbol{Q}}\tilde{\boldsymbol{\theta}}$ does not have a unique solution as the rank of $\tilde{\boldsymbol{Q}}$ is only three. This is because the third and fourth columns of $\tilde{\boldsymbol{Q}}$ are a count of the number of on and off mirrors for each pattern which is redundant information. To correct this, we need to either add in more information to the $\tilde{\boldsymbol{Q}}$ matrix or reduce the number or parameters. It is reasonable to assume that ambient sources have minimal impact through off-state mirrors. Therefore, we replace β_1 and β_0 with a single parameter β and remove the fourth column from $\tilde{\boldsymbol{Q}}$. This yields our system for Model 3,

$$\boldsymbol{g} = \underbrace{\left(\alpha_1\boldsymbol{P} + \alpha_0\boldsymbol{P}^C\right)\boldsymbol{x}}_{\boldsymbol{\Phi}} + \beta\boldsymbol{P}\mathbf{1}, \tag{4.30}$$

which can be rewritten as the linear system

$$\boldsymbol{g} = \underbrace{\begin{bmatrix} \boldsymbol{P}\boldsymbol{x} & \boldsymbol{P}^C\boldsymbol{x} & \boldsymbol{P}\mathbf{1} \end{bmatrix}}_{\boldsymbol{Q}} \underbrace{\begin{bmatrix} \alpha_1 \\ \alpha_0 \\ \beta \end{bmatrix}}_{\boldsymbol{\theta}}. \tag{4.31}$$

and solved via the least squares estimator in Equation (4.24).

With estimated parameters $\hat{\alpha}_0$, $\hat{\alpha}_1$, and $\hat{\beta}$, the estimated measurement matrix becomes

$\hat{\boldsymbol{\Phi}} = \hat{\alpha}_1 \boldsymbol{P} + \hat{\alpha}_0 \boldsymbol{P}^C$, and a test signal $\boldsymbol{g}_{test}$ can be used to reconstruct a target $\boldsymbol{x}_{test}$ as

$$\hat{\boldsymbol{x}}_{test} = \text{rvm}(\boldsymbol{g}_{test} - \hat{\beta}\boldsymbol{P}\mathbf{1}, \hat{\boldsymbol{\Phi}}), \tag{4.32}$$

where the first argument to the rvm reconstruction now includes a bias correction.

4.6 Model 4: Spatial Gain Gradients

The final calibration model proposed addresses observed spatial variations in DMD gains. Reconstructed images using the earlier calibration models depict variations in the brightness of target points that are known to be of uniform illumination. For example, Figure 4.2 presents a reconstruction of the letter "U", where the constituent LEDS were all of equal brightness, yet the reconstruction exhibits a horizontal dim-to-bright gradient. This is likely caused by defects with the DMD mirrors and by the optical system elements not being perfectly on axis. Others [14] have also noticed that the mirror reflectance is not uniform.

While we could model independent gains per mirror, the number of unknown parameters would be large and would require excessive training data. We propose to address the spatial variance by adding a spatially varying gain across the mirrors modeled by a ramp-shaped 2D gradient. The gradient is consistent with our observations (e.g., Figure 4.2) and constrains the number of parameters.

In Model 2, we introduced α_0 as a constant gain for the off state mirrors and α_1 as a constant gain for the on state mirrors. We now let the values of α_0 and α_1 depend on the discrete 2D mirror location (x_i, y_j), where the rows are indexed by $j = 1, \ldots, m$, and the columns are indexed by $i = 1, \ldots, n$:

$$\alpha_0(x_i, y_j) = \alpha_0^x x_i + \alpha_0^y y_j + \alpha_0^1, \tag{4.33}$$

$$\alpha_1(x_i, y_j) = \alpha_1^x x_i + \alpha_1^y y_j + \alpha_1^1. \tag{4.34}$$

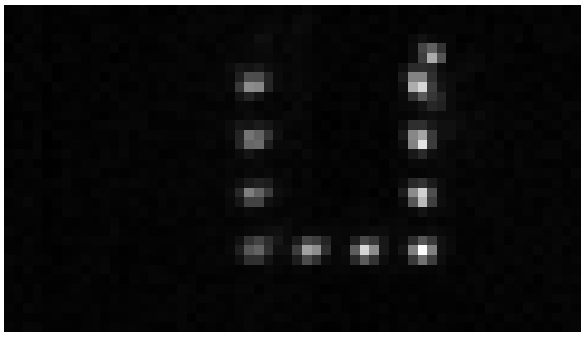

Figure 4.2: Without compensation, reconstructions depict spatially variant mirror gains seen here as a dim-to-bright gradient across the image.

The values of $\alpha_0(x_i, y_j)$ and $\alpha_1(x_i, y_j)$ are dependent on six calibration parameters. α_0^x and α_1^x are the ramp function gains in the x direction for the off and on state mirrors, respectively. α_0^y and α_1^y are the ramp function gains in the y direction. α_0^1 and α_1^1 are constant gain components for the off and on state mirrors that are independent of mirror location.

Because arbitrary scaling of the (x, y) mirror coordinates can be absorbed into the gains, we can—without loss of generality—define

$$x_i = \frac{i}{n}, \quad i = 1, \ldots, n \tag{4.35}$$

and

$$y_j = \frac{j}{m}, \quad j = 1, \ldots, m \tag{4.36}$$

where n is the number of columns in the DMD mirror array, and m is the number of rows. Further, it is convenient to define $m \times n$ gain matricies $\boldsymbol{A}_0$ and $\boldsymbol{A}_1$, whose (i, j) entries are

$\alpha_0(x_i, y_j)$ and $\alpha_1(x_i, y_j)$, respectively. Then, the horizontal gradient matrix

$$\boldsymbol{D}_x = \begin{bmatrix} \frac{1}{n} & \frac{2}{n} & \dots & 1 \\ \frac{1}{n} & \frac{2}{n} & \dots & 1 \\ & & \vdots & \\ \frac{1}{n} & \frac{2}{n} & \dots & 1 \end{bmatrix} \tag{4.37}$$

and vertical gradient matrix

$$\boldsymbol{D}_y = \begin{bmatrix} \frac{1}{m} & \frac{1}{m} & \dots & \frac{1}{m} \\ \frac{2}{m} & \frac{2}{m} & \dots & \frac{2}{m} \\ & & \vdots & \\ 1 & 1 & \dots & 1 \end{bmatrix} \tag{4.38}$$

form 2D basis functions for $\boldsymbol{A}_0$ and $\boldsymbol{A}_1$, along with $(\mathbf{1}_m \mathbf{1}_n^T)$, a matrix of ones with the same dimensions. The spatial gain matrices may then be expressed as

$$\boldsymbol{A}_0 = \alpha_0^x \boldsymbol{D}_x + \alpha_0^y \boldsymbol{D}_y + \alpha_0^1 (\mathbf{1}_m \mathbf{1}_n^T) \tag{4.39}$$

and

$$\boldsymbol{A}_1 = \alpha_1^x \boldsymbol{D}_x + \alpha_1^y \boldsymbol{D}_y + \alpha_1^1 (\mathbf{1}_m \mathbf{1}_n^T) \tag{4.40}$$

which provide a 2D linear gradients (for on and off) in the gain, with arbitrary scaling and orientation, across the DMD array. In Figure 4.3, we illustrate this with an $n = m = 20$ example using grey-scale images to represent the matrices. In the example, gradient directions are depicted by the green arrows. The horizontal gradient is scaled by $\alpha_x = 0.3$, and the vertical gradient by $\alpha_y = -0.7$ to yield the diagonal gain gradient across the DMD.

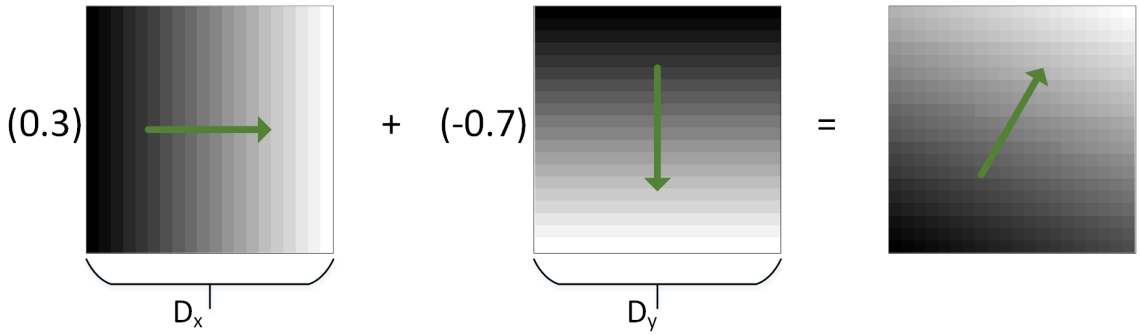

Figure 4.3: Spatial gradient example: linear combinations of the horizontal and vertical gradients produce spatial DMD gain profiles with with arbitrary scale and orientation.

For a target image $\boldsymbol{x}$, the kth measurement in Model 4 may be written as

$$g_k = \sum_i \sum_j (\boldsymbol{A}_1 \odot [\boldsymbol{p}_k] \odot [\boldsymbol{x}] + \boldsymbol{A}_0 \odot [\boldsymbol{p}_k^C] \odot [\boldsymbol{x}])_{i,j}, \tag{4.41}$$

where $\odot$ denotes the Hadamard (elementwise) product. For the mathematical convenience of evaluating multiple measurements over many patterns, it is useful to (columnwise) vectorize the spatial gains and gradients as

$$\boldsymbol{\alpha}_0 = \text{vec}(\boldsymbol{A}_0), \quad (N \times 1) \tag{4.42}$$

$$\boldsymbol{\alpha}_1 = \text{vec}(\boldsymbol{A}_1), \quad (N \times 1) \tag{4.43}$$

$$\boldsymbol{d}_x = \text{vec}(\boldsymbol{D}_x), \quad (N \times 1) \tag{4.44}$$

$$\boldsymbol{d}_y = \text{vec}(\boldsymbol{D}_x), \quad (N \times 1). \tag{4.45}$$

The entire $K \times 1$ measurement vector may now be written as

$$\boldsymbol{g} = ((\boldsymbol{1}_K \boldsymbol{\alpha}_1^T) \odot \boldsymbol{P} + (\boldsymbol{1}_K \boldsymbol{\alpha}_0^T) \odot \boldsymbol{P}^C)\boldsymbol{x} \tag{4.46}$$

$$= \underbrace{((\boldsymbol{1}_K(\alpha_1^x \boldsymbol{d}_x + \alpha_1^y \boldsymbol{d}_y + \alpha_1^1 \boldsymbol{1}_N)^T) \odot \boldsymbol{P} + (\boldsymbol{1}_K(\alpha_0^x \boldsymbol{d}_x + \alpha_0^y \boldsymbol{d}_y + \alpha_0^1 \boldsymbol{1}_N)^T) \odot \boldsymbol{P}^C)}_{\boldsymbol{\Phi}} \boldsymbol{x} \tag{4.47}$$

In order to solve for the calibration coefficients $\tilde{\boldsymbol{\theta}} = [\alpha_1^1, \alpha_1^x, \alpha_1^y, \alpha_0^1, \alpha_0^x, \alpha_0^y]^T$ when $\boldsymbol{g}$ and $\boldsymbol{x}$ are known, we re-write (4.47) in the linear form

$$\boldsymbol{g} = \underbrace{[\boldsymbol{q}_1\ \boldsymbol{q}_2\ \boldsymbol{q}_3\ \boldsymbol{q}_4\ \boldsymbol{q}_5\ \boldsymbol{q}_6]}_{\tilde{\boldsymbol{Q}}}\tilde{\boldsymbol{\theta}}, \tag{4.48}$$

where

$$\boldsymbol{q}_1 = \boldsymbol{P}\boldsymbol{x}, \tag{4.49}$$

$$\boldsymbol{q}_2 = ((\mathbf{1}_K \boldsymbol{d}_x^T) \odot \boldsymbol{P})\boldsymbol{x}, \tag{4.50}$$

$$\boldsymbol{q}_3 = ((\mathbf{1}_K \boldsymbol{d}_y^T) \odot \boldsymbol{P})\boldsymbol{x}, \tag{4.51}$$

$$\boldsymbol{q}_4 = \boldsymbol{P}^C\boldsymbol{x}, \tag{4.52}$$

$$\boldsymbol{q}_5 = ((\mathbf{1}_K \boldsymbol{d}_x^T) \odot \boldsymbol{P}^C)\boldsymbol{x}, \tag{4.53}$$

$$\boldsymbol{q}_6 = ((\mathbf{1}_K \boldsymbol{d}_y^T) \odot \boldsymbol{P}^C)\boldsymbol{x}, \tag{4.54}$$

As in the case of Model 3, $\tilde{\boldsymbol{Q}}$ in Equation (4.48) is rank deficient—only having a rank of four. It is a reasonable to assume that the gain variance across the off-state mirrors is negligible. Therefore, we model $\boldsymbol{\alpha}_0$ as simply a constant, α_0^1, and reduce our parameter count to four

$$\boldsymbol{\theta} = [\alpha_1^1, \alpha_1^x, \alpha_1^y, \alpha_0^1]^T \tag{4.55}$$

yielding a full-rank system of equations

$$\boldsymbol{g} = \boldsymbol{Q}\boldsymbol{\theta}, \tag{4.56}$$

where

$$\boldsymbol{Q} = [\boldsymbol{q}_1\ \boldsymbol{q}_2\ \boldsymbol{q}_3\ \boldsymbol{q}_4]. \tag{4.57}$$

From the least-squares estimates of the calibration parameters, $\hat{\boldsymbol{\theta}} = (\boldsymbol{Q}^T\boldsymbol{Q})^{-1}\boldsymbol{Q}^T\boldsymbol{g}$, we obtain from (4.47) the estimated measurement matrix

$$\hat{\boldsymbol{\Phi}} = \boldsymbol{\Phi}(\hat{\boldsymbol{\theta}}) \tag{4.58}$$

$$= (\hat{\alpha}_1^x \mathbf{1}_K \boldsymbol{d}_x^T + \hat{\alpha}_1^y \mathbf{1}_K \boldsymbol{d}_y^T + \hat{\alpha}_1^1 \mathbf{1}_K \mathbf{1}_N)^T) \odot \boldsymbol{P} + \hat{\alpha}_0^1 \boldsymbol{P}^C. \tag{4.59}$$

Recalling the RVM syntax of Section 2.3, a test signal $\boldsymbol{g}_{test}$ can be used to reconstruct an unknown target $\boldsymbol{x}_{test}$ as

$$\hat{\boldsymbol{x}}_{test} = \text{rvm}(\boldsymbol{g}_{test}, \hat{\boldsymbol{\Phi}}). \tag{4.60}$$

4.7 Calibration using Multiple targets

In the preceding sections, only a single target-measurement pair $(\boldsymbol{x}, \boldsymbol{g})$ was used for calibration. However, in all four models the calibration parameters $\boldsymbol{\theta}$ satisfied a linear set of equations

$$\boldsymbol{g} = \boldsymbol{Q}(\boldsymbol{x})\boldsymbol{\theta}. \tag{4.61}$$

In (4.61), we explicitly indicate the dependence of the calibration matrix $\boldsymbol{Q}$ on the known calibration target $\boldsymbol{x}$. In many cases, more than one target-measurement pair is available for use in estimating the parameters $\boldsymbol{\theta}$. For T calibration pairs $\{(\boldsymbol{x}_t, \boldsymbol{g}_t) : t = 1, \ldots, T\}$, a

straightforward extension of (4.61) yields a linear system employing all of the calibration data

$$\underbrace{\begin{bmatrix} \boldsymbol{g}_1 \\ \vdots \\ \boldsymbol{g}_T \end{bmatrix}}_{\bar{\boldsymbol{g}},\,(TK\times 1)} = \underbrace{\begin{bmatrix} \boldsymbol{Q}(\boldsymbol{x}_1) \\ \vdots \\ \boldsymbol{Q}(\boldsymbol{x}_T) \end{bmatrix}}_{\bar{\boldsymbol{Q}},\,(Tk\times s)} \underbrace{\boldsymbol{\theta}}_{(s\times 1)}, \tag{4.62}$$

where s is the number of calibration parameters in the particular model being considered. Hence, standard least squares provides parameter estimates using all of the calibration data via the augmented system

$$\hat{\boldsymbol{\theta}} = (\bar{\boldsymbol{Q}}^T\bar{\boldsymbol{Q}})^{-1}\bar{\boldsymbol{Q}}^T\bar{\boldsymbol{g}}. \tag{4.63}$$

Results

5.1 Generated Testing Data

We use three letter targets to test our compressive sensing calibration models. Figure 5.1 shows each target as a 16x32 image. These images are displayed on the LED board where each pixel represents a single LED light. The black pixels are turned off and white pixels turn on a white LED. Each letter is formed from seven to ten LEDs.

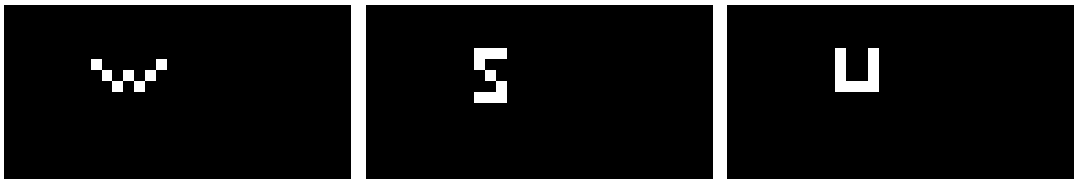

(a) W target (b) S Target (c) U Target

Figure 5.1: WSU LED targets

For each target we collected 2000 measurements to use for testing as described in Section 3.1. The same 2000 randomly generated patterns were used for each target. It took approximately 5 hours to collect data for each target.

5.2 Generating Truth Data

A truth signal is needed to calibrate the models and measure the error present in the reconstruction. Unfortunately, it was not possible to perfectly align our LED board with the

DMD mirrors in a constant ratio. Each LED mapped to a number of mirrors on the DMD. To help understand this relationship we performed a raster scan with the DMD. We turned each mirror on, one at a time, and took a measurement using the camera. This process was repeated for each LED target. We scaled the measurements between zero and one and displayed the combined measurements as an image. The WSU raster scans are shown in Figure 5.2. Note that the entire LED board was not in the field of view for the DMD mirrors. The 60x34 images in Figure 5.2 show the field of view and are the same scale as the final reconstructed images.

We observed that each LED illuminated approximately nine mirrors with most of the power concentrated on the center mirror. We modeled this with the cross patterns shown in Figure 5.3 which uses a value of 1 at the center, 0.5 on the edges, and 0.25 on the corners. In order to create our simulated truth images we manually mapped each LED to a pixel location by placing a cross at the brightest point in the raster scan and interpolating values for the LEDs which were not in the test set. Figure 5.4 shows our derived truth images.

The raster scans show a large bright spot in the upper right corner. This noisy artifact was present in all of our collected data and was an optical aberration that did represent actual light reflected from the mirrors. Since this noise source was effecting our calibration results, particularly the gradients in Model 4, we chose to add this artifact to the truth signal by placing six 0.25 valued gray pixels at the observed locations.

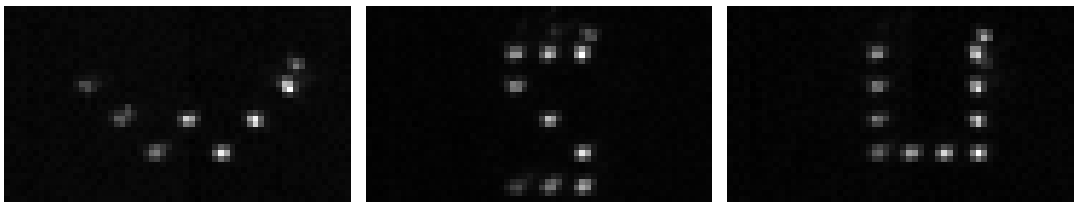

(a) W target raster scan (b) S Target raster scan (c) U Target raster scan

Figure 5.2: WSU LED targets raster scans

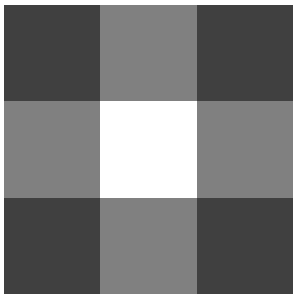

Figure 5.3: For ground truth images, a cross pattern over nine mirrors was used for each LED

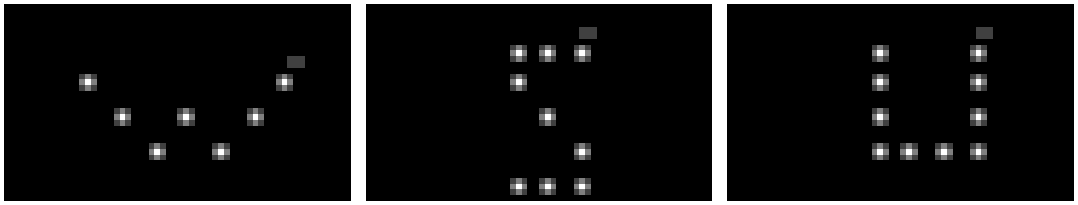

(a) W derived truth (b) S derived truth (c) U derived truth

Figure 5.4: Derived "W", "S", and "U" ground through targets

5.3 Calibration Issues

Forty random dot targets were created to use for calibration. Figure 5.5 shows 16 of the Forty random targets used. There were 10 random targets for each class that had one, two, three, or four LEDs turned on. 500 measurements were taken for each target and the same 500 random patterns were used for each target. However, there were some interruptions during the data collection process and some targets have an incomplete number of measurements or no measurements at all. 16680 total measurements were taken from 33 calibration dot targets.

After data was collected, we discovered that the random calibration patterns were not representative of our letter test targets. Figure 5.6 shows which LEDs were turned on for each target. Sub-figure 5.6(d) shows a count of the total number of targets that used each LED for all of the calibration dot targets. The LEDs are not equally represented in the test data set, and some LEDs are missing entirely. This made it difficult to estimate the gradient required for Model 4.

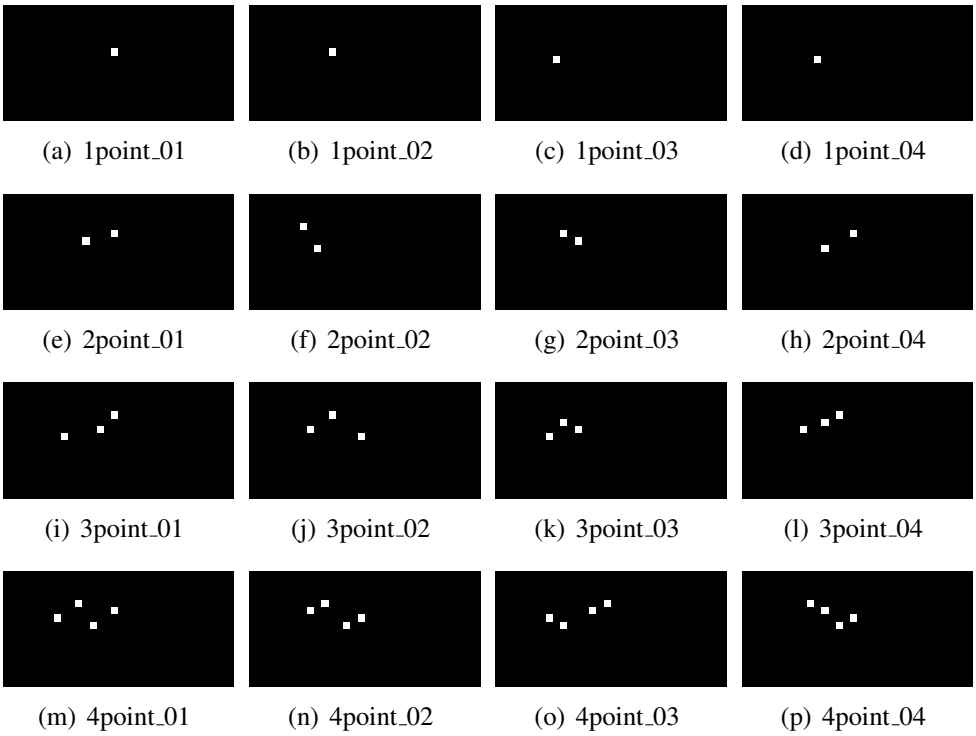

(a) 1point_01 (b) 1point_02 (c) 1point_03 (d) 1point_04

(e) 2point_01 (f) 2point_02 (g) 2point_03 (h) 2point_04

(i) 3point_01 (j) 3point_02 (k) 3point_03 (l) 3point_04

(m) 4point_01 (n) 4point_02 (o) 4point_03 (p) 4point_04

Figure 5.5: Sample LED calibration targets

Since we did not feel that our calibration data was representative of our test data, we used a single letter, U, for calibration and used those parameters to reconstruct the W and S targets.

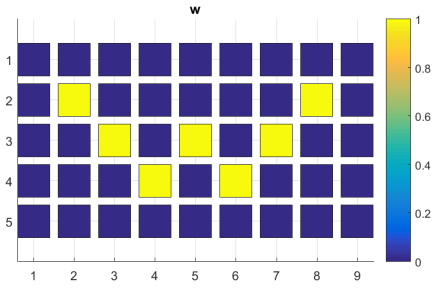

(a) LEDs used in W target

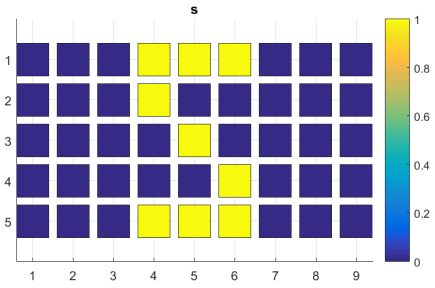

(b) LEDs used in S target

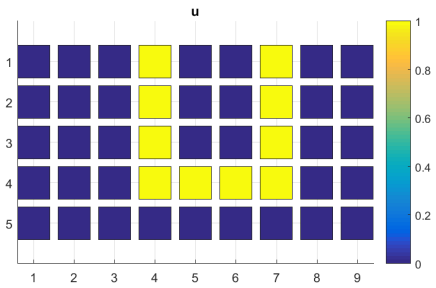

(c) LEDs used in U target

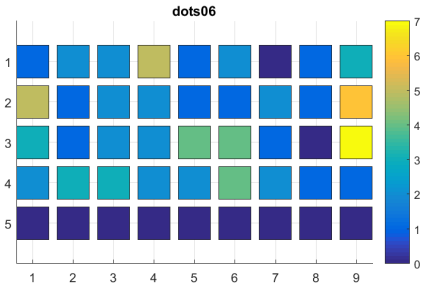

(d) LEDs used in dot calibration targets

Figure 5.6: Frequency of LEDs in calibration and testing data set

5.4 Calibration Results

In this section, we examine how well the modeled data, $\boldsymbol{g}_{modeled} = \hat{\boldsymbol{\Phi}}\boldsymbol{x}$, matches the noisy measured data $\boldsymbol{g}$ for each of our calibration models. Figure 5.7 shows the normalized calibration error plot for Model 1, the scalar gain model. While we label this plot as "error", what we are truly plotting is a distance, d, between $\boldsymbol{g}_{modeled}$ and $\boldsymbol{g}$,

$$d = \frac{||\boldsymbol{g_{modeled}} - \boldsymbol{g}||_2}{||\boldsymbol{g}||_2}. \tag{5.1}$$

It is this distance that is minimized in the calibration process. For Model 1 we can calculate d for a range of parameters and plot the error for each parameter value. In Sub-figure 5.7(a) we use the measurements taken from the W target and in Sub-figure 5.7(b) we use the

measurements taken from the S target. The magenta x marks the parameter found from Model 1 calibration using the U target. The error at this point can be compared to the error at the black triangle marking the error with no calibration, and the green circle marking the minimum possible error for that target. The minimum error would be found by using the same target for calibration and testing. This point has the best possible parameters for the given target. The uncalibrated point just assumes that $\alpha = 1$ which has no effect on the measurement matrix. Calibrating with the U target comes fairly close to the optimal parameter values for both test targets and offers significance improvements compared to the uncalibrated measurements.

Figure 5.8 shows the normalized error plot for Model 2, on- and off state gains, calibration for each letter target. Here we have two parameters and we use color to indicate the error at each parameter value combination. The vertical line of $\alpha_0 = 0$ matches the Model 1 plots in Figure 5.7. We plot the same 2 points, no calibration and Model 1 calibration, and compare to the parameters chosen when calibrating with the U target, marked with a yellow plus sign. We also mark the minimum possible error for each with a green circle. We see that the parameters found when calibrating with the U target are fairly close to the optimal parameters for each target and that Model 2 offers a slight improvement over Model 1.

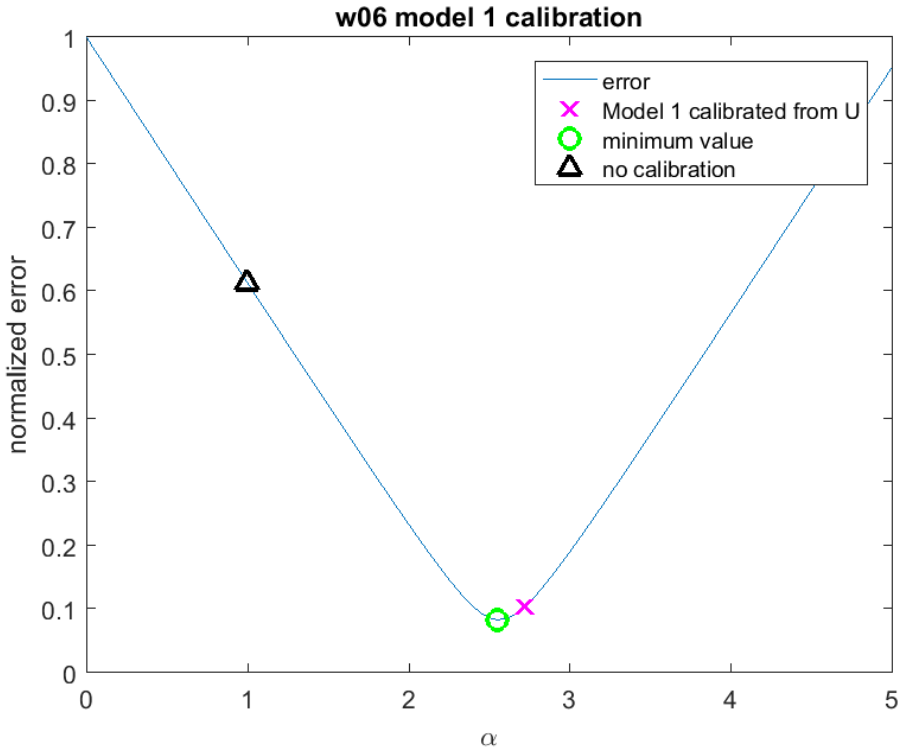

(a) Model 1 calibration error plot for W

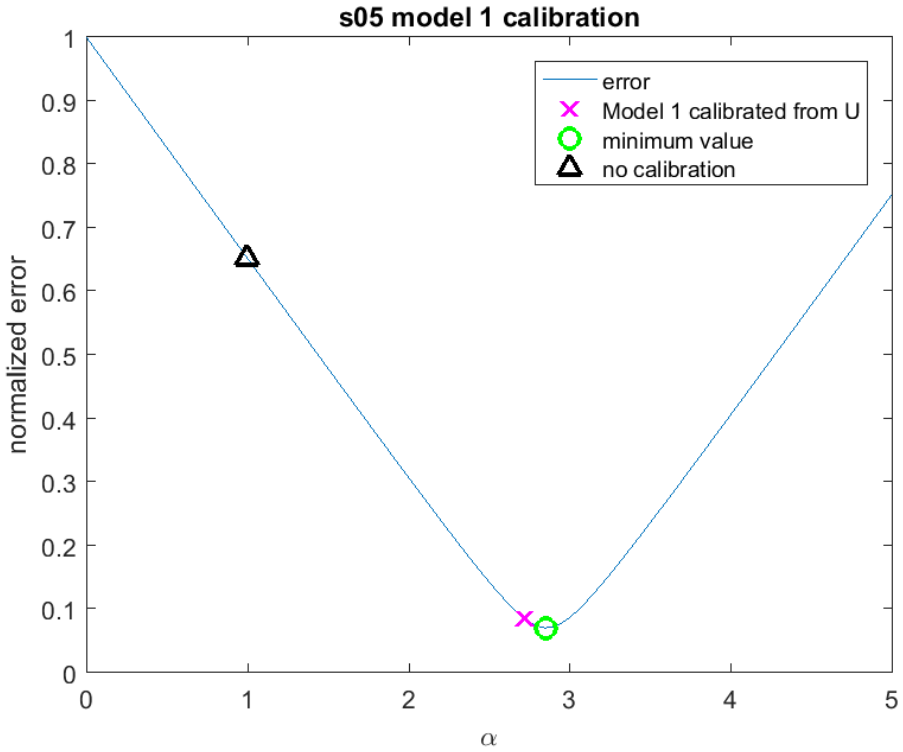

(b) Model 1 calibration error plot for S

Figure 5.7: Model 1 parameter space

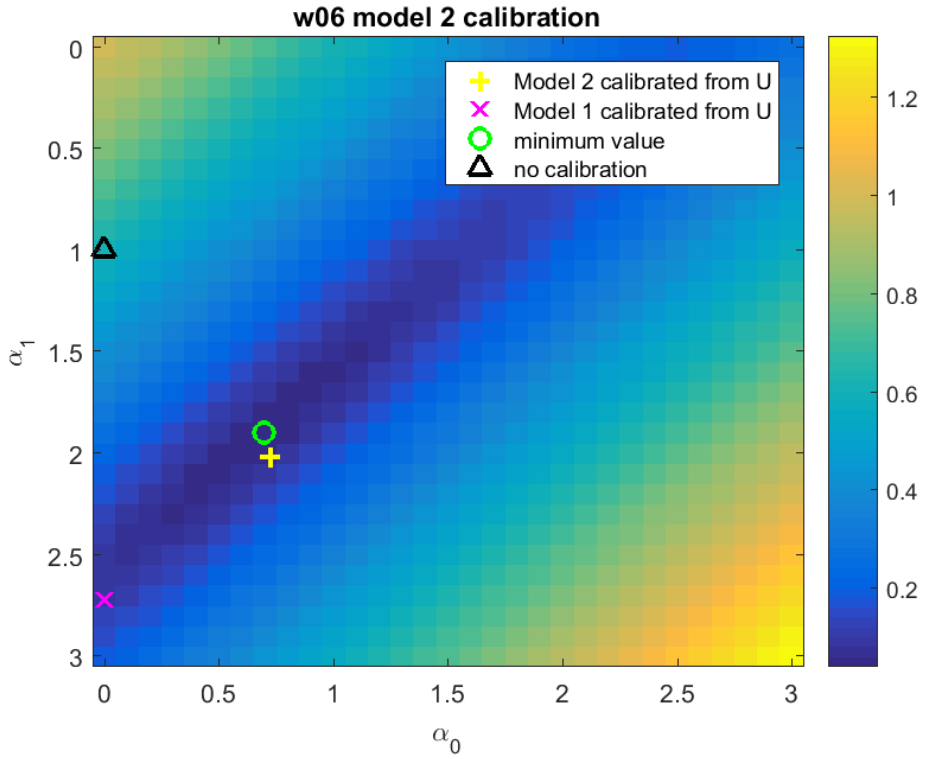

(a) Model 2 calibration error plot for W target

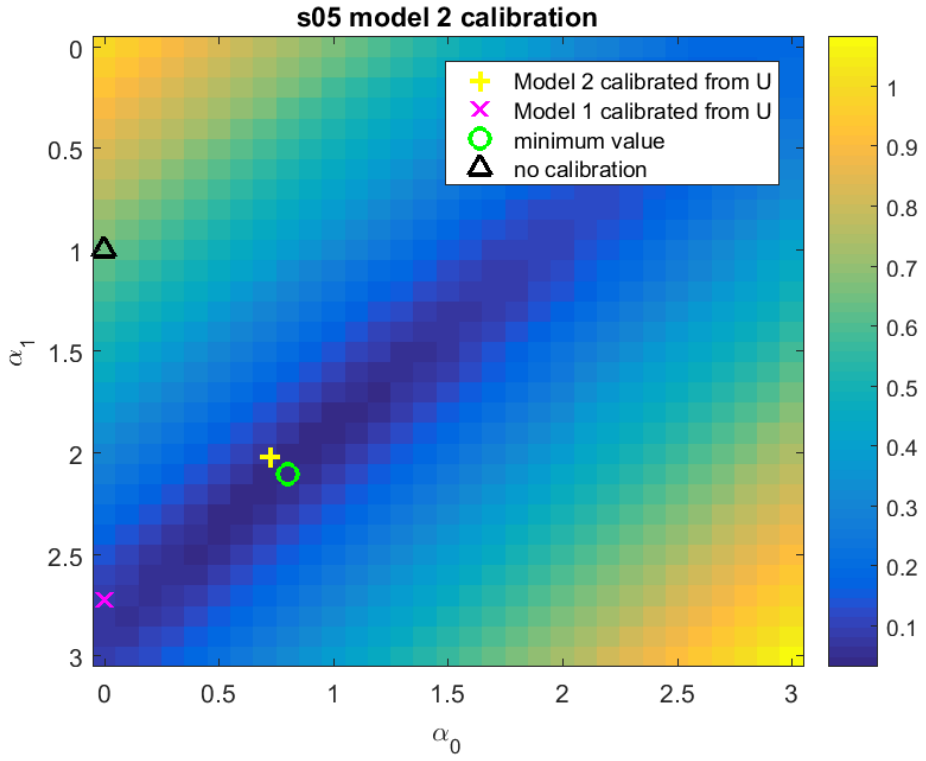

(b) Model 2 calibration error plot for S target

Figure 5.8: Model 2 parameter space

Models 3 and 4 have additional parameters and are therefore, harder to visualize. Table 5.1 shows the error for the W and S target when using the parameters listed. These parameters were calibrated from the U target. The optimal values and their error for the W and S target are included for reference in Table 5.2 and Table 5.3. The error for the optimal values (column d in Table 5.2 and Table 5.3) decreases as the number of calibration parameters increase. This relation is not always true for the calibrated models (columns d_W and d_S in Table 5.1) although at this point the error differences are very small.

Table 5.1: Calibration results using U for calibration and W and S for testing

	d_W	d_S	$\boldsymbol{\alpha_1}$	$\boldsymbol{\alpha_0}$	$\boldsymbol{\beta}$	$\boldsymbol{\alpha_x}$	$\boldsymbol{\alpha_y}$
Model 0	a	b	-	-	-	-	-
Model 1	0.1030	0.0853	2.72	-	-	-	-
Model 2	0.0726	0.0585	2.03	0.73	-	-	
Model 3	0.2191	0.0329	1.50	0.25	0.02	-	
Model 4	0.0400	0.1015	0.44	0.73	-	2.60	0.07

Table 5.2: Optimal calibration results for the W target

	d	$\boldsymbol{\alpha_1}$	$\boldsymbol{\alpha_0}$	$\boldsymbol{\beta}$	$\boldsymbol{\alpha_x}$	$\boldsymbol{\alpha_y}$
Model 0		-	-	-	-	-
Model 1	0.0831	2.56	-	-	-	-
Model 2	0.0410	1.89	0.69	-	-	-
Model 3	0.0400	1.35	0.18	0.02	-	-
Model 4	0.0348	1.10	0.69	-	2.08	-0.78

Table 5.3: Optimal calibration results for the S target

	d	$\boldsymbol{\alpha_1}$	$\boldsymbol{\alpha_0}$	$\boldsymbol{\beta}$	$\boldsymbol{\alpha_x}$	$\boldsymbol{\alpha_y}$
Model 0		-	-	-	-	-
Model 1	0.0704	2.86	-	-	-	-
Model 2	0.0321	2.13	0.75	-	-	-
Model 3	0.0304	1.43	0.11	0.03	-	-
Model 4	0.0270	-0.90	0.74	-	5.05	0.65

Figure 5.9 visually compares the modeled data, $\boldsymbol{g}_{modeled}$, with the noisy measured data, $\boldsymbol{g}$. The measurements shows here are the the 33 calibration dot targets. The x-axis an index of the measurement and most targets have around 500 measurements each. In the top subplot, the average measurement increase based on the target class. The first measurements come from targets with 1 LED on and the later come from targets with 4 LEDS on. The average value of all measurements for each target varies based on the target.

Models 1-3 each scale the predicted values closer to the actual measurements, but only Model 4 accounts for the variance based on which LEDs are turned on.

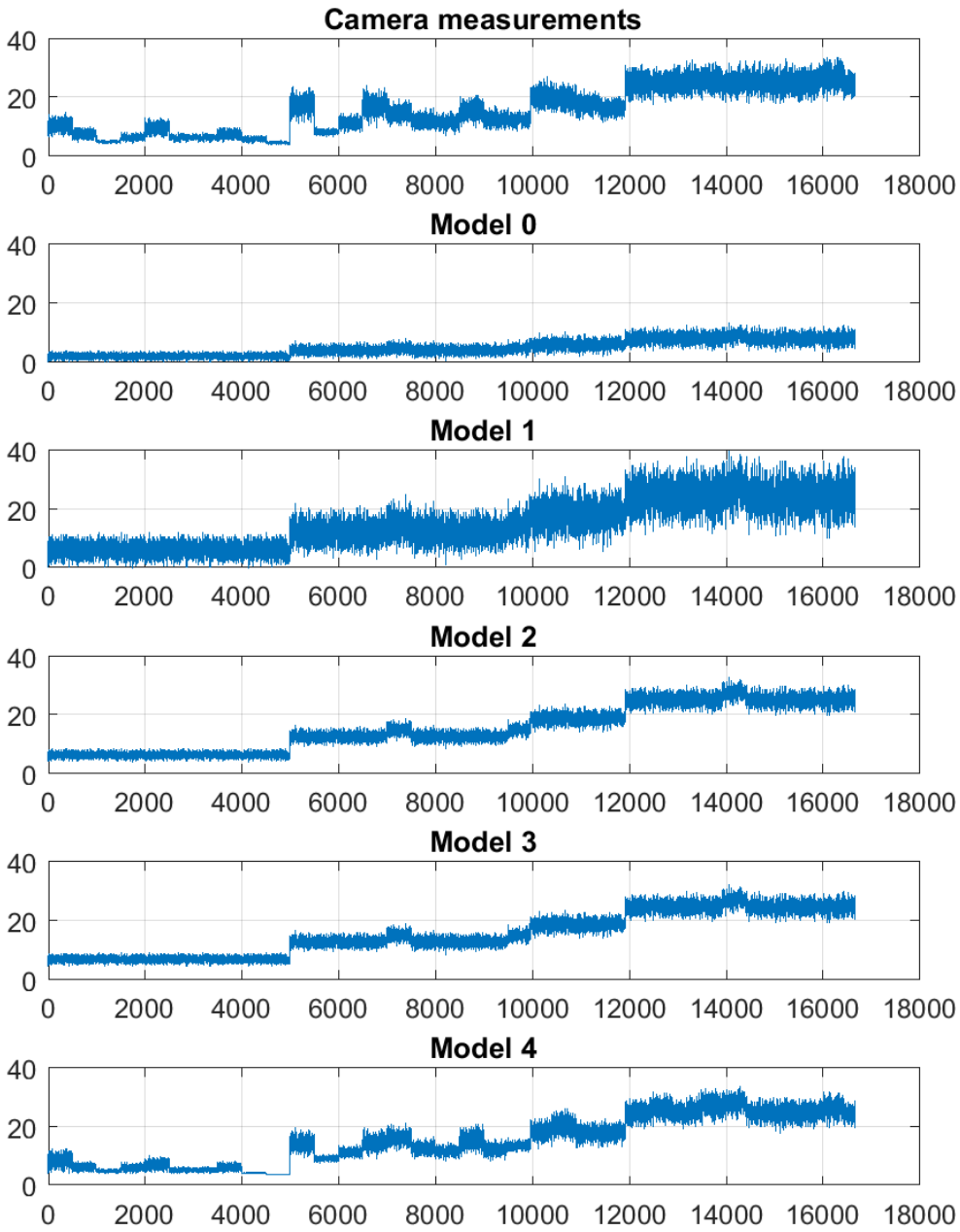

Figure 5.9: Comparison of raw camera measurements versus measurements modeled through the calibration process

Model 2 and Model 3 produce very similar modeled signals. Model 3 produces the same measurement matrix, $\hat{\mathbf{\Phi}}$, as model 2 and adjusts the measurement vector by a factor

of $\beta \boldsymbol{P1}$. For each camera measurement k, Model 3 will subtract β times the number of mirrors set to on while that measurement was collected. If this adjustment factor was the same for each measurement, i.e., the same number of mirrors where on , then this constant term could be absorbed into the gains α_0 and α_1. Since the calibrated β parameter (see Table 5.1) is relatively small compared to the mean of the measured image amplitude and each mirror is equally likely to be on or off for our data, this adjustment factor is close to constant and the signal model difference between Model 2 and Model 3 is very small. Figure 5.10 shows these results for the first 500 measurements of the W target. The top subplot shows the adjustment factor $\beta \boldsymbol{P1}$ versus the measurement index. Compared to the signal measurement vector in the middle subplot the adjustment factor is relatively constant. The bottom subplot shows the measurement vector after adjustment. We propose that this model would provide a larger difference from Model 2 if the expected number of on mirrors varied more from pattern to pattern.

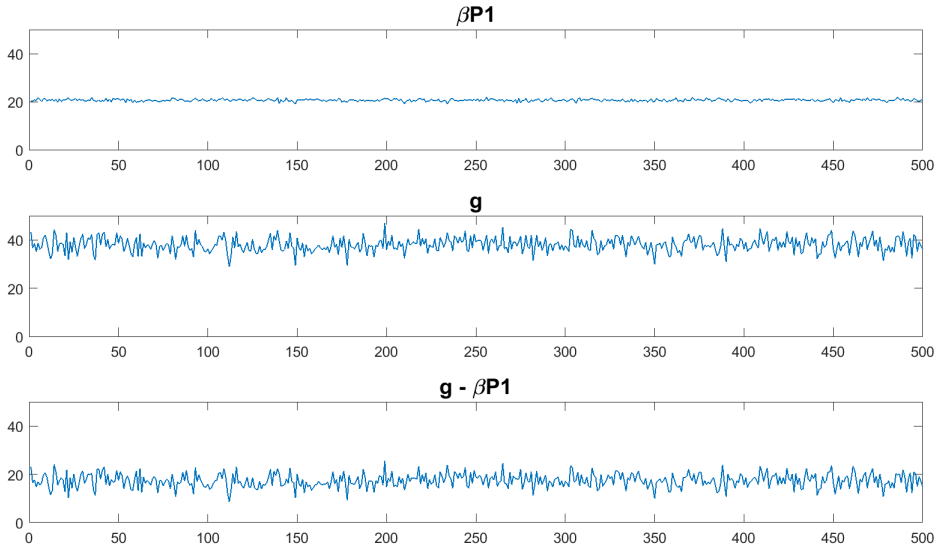

Figure 5.10: Effect of β parameter on Model 3

5.5 Reconstruction Results

We use the U target to calculate our calibration parameters, and then reconstruct the W and S targets using a subset of the measurements taken. We reconstruct using 2, 5, 10, 15, 20, 30, 40, 50 and 98 percent of length of the target signal which is $N = 2040$. RVM will often return a noisy result with large spikes that do not match to the target signal. However, the level of uncertainty for these spikes is high.

Figure 5.11 shows the W target reconstructed from $K = 612$ measurements. The target signal is shown in the top subplot with the reconstructed signal shown below in the second subplot. Note the large negative spikes at the beginning of the reconstruction not present in the target signal. The third subplot adds error bars on to the reconstruction and the magnitude of the these error bars is shown in the bottom subplot. The magnitude of the error bars for the erroneous spikes at the beginning of the vector is much larger that the error bars for the spikes present in the target signal.

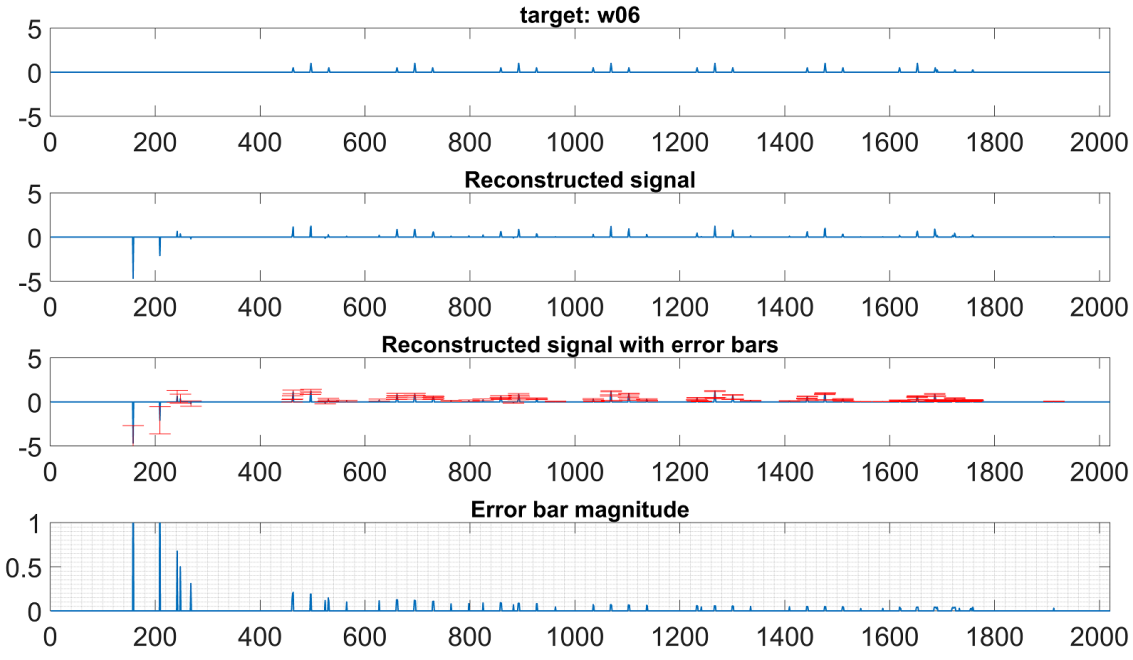

Figure 5.11: Noisy reconstructed signal with error bars showing uncertainty

One of the advantages of the Bayesian approach to CS is the presentation of uncer-

tainty with signal estimates. We can choose a uncertainty threshold and set any reconstructed point with an error above that threshold to zero, removing it from the reconstruction. We found that a threshold of 0.3 removed most of the noise without loosing too many points present in the target signal. We use the same threshold for all calibration models and reconstruction levels.

We can reshape our reconstructed target signal vector, $\hat{\boldsymbol{x}}$ as a matrix with the dimensions of the DMD (60×34). Then we can display the result as an image altering scaling the values between zero and one. Figure 5.13 shows the visual reconstruction results for the W target using all five calibration models and for a range of measurement counts, $K = 204, 306, 408, 612, 816, 1020, 2000$. The same results are shown for the S target in Figure 5.14. m0-m4 refer to the calibration model used for the reconstruction. The number of measurements used for the reconstruction is listed in the sub figure caption for each row.

Models 2, 3, and 4 start to produce a good reconstruction using only 15 to 20 percent of the measurements. The uncalibrated Model 0 and the baseline Model 1 do not begin to resolve the target until 30 percent of the measurements are used. At this level, the reconstruction is significantly noisier compared to the other models and some LED are missed entirely. When nearly all measurements are used all LEDs are present but the resulting reconstruction is still very noisy.

The visual differences between Models 2 and 3 are very small. As discussed in Section 5.4, this was expected for our data set. Both models offer significantly cleaner reconstructions compared to no calibration and the baseline model.

When we examine the visual results for Model 4 we expect to see a more equal intensity value for each LED present in the reconstruction. This is best seen in the reconstructions for the W target. In the Model 3 reconstruction, the LEDs on the left side are dimmer than those on the right. When Model 4 is used, the intensity values are much more uniform. The top left LED is possibly a bit too bright. Figure 5.12 shows this comparison at a thirty percent reconstruction.

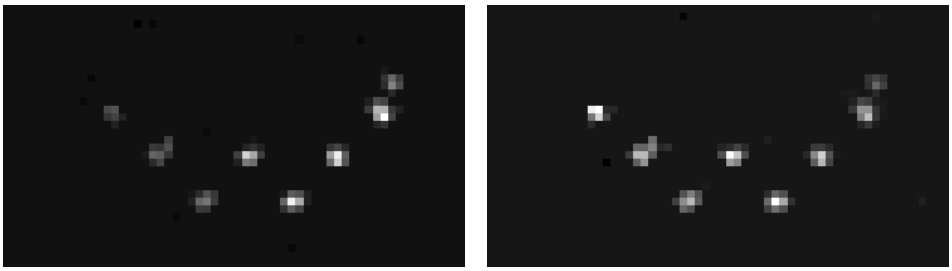

(a) W reconstructed with Model 3 (b) W reconstructed with Model 4

Figure 5.12: Comparing Model 3 and Model 4 at K = 612 (30%)

Model 4 also equalized the S target LEDs from left to right although the effect is less severe since it is a thinner target. The bottom row of the S is still too dim compared to the other LEDs. The bottom row of the LEDs were at the very edge of the mirror array. We hypothesize that these points were lower intensity due to some light being lost to the non-reflective edges of the mirror array. This could not be modeled by our 2D linear step function gradient.

(a) Reconstructed from K = 10% N = 204 (90% undersampling)

(b) Reconstructed from K = 15% N = 306 (85% undersampling)

(c) Reconstructed from K = 20% N = 408 (80% undersampling)

(d) Reconstructed from K = 30% N = 612 (70% undersampling)

(e) Reconstructed from K = 40% N = 816 (60% undersampling)

(f) Reconstructed from K = 50% N = 1020 (50% undersampling)

(g) Reconstructed from K = 98% N = 2000 (2% undersampling)

Figure 5.13: Image reconstruction for W target

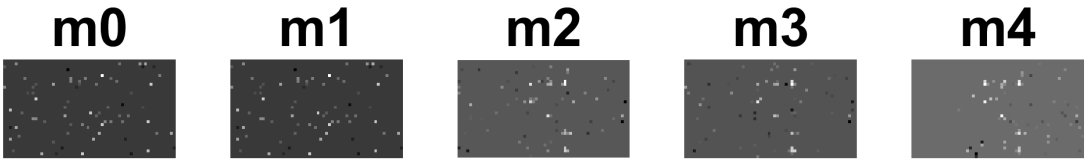

(a) Reconstructed from K = 10% N = 204 (90% undersampling)

(b) Reconstructed from K = 15% N = 306 (85% undersampling)

(c) Reconstructed from K = 20% N = 408 (80% undersampling)

(d) Reconstructed from K = 30% N = 612 (70% undersampling)

(e) Reconstructed from K = 40% N = 816 (60% undersampling)

(f) Reconstructed from K = 50% N = 1020 (50% undersampling)

(g) Reconstructed from K = 98% N = 2000 (2% undersampling)

Figure 5.14: Image reconstruction for S target

Our observations are consistent with Candès who demonstrates that typically the number of required measurements is equal to 4x the level of sparsity [17]. We have approximately 120 "spikes" in our targets and we start seeing good reconstruction results at 408 samples. In an earlier paper, Candès formally defines the number of required oversampling factor to be $\log N$ for a Bernolli +/- 1 distribution [18]. Our performance with patterns using 0 or 1 does not appear to significantly increase the number or required measurements.

Visual inspection of the reconstruction results is a subjective process so we introduce a reconstruction error metric to provide more objective results. Reconstruction error is measured by the normalized squared error between the derived truth image and the reconstructed image

$$e = \frac{||\hat{\boldsymbol{x}} - \boldsymbol{x}||_2}{||\boldsymbol{x}||_2}. \tag{5.2}$$

This is a limited metric since our truth data is not perfectly aligned with the actual location of the LEDs. A correctly reconstructed point may be shifted by a pixel and add to the error measurement. However, this metric still gives us some insight into the performance of our calibration models.

Figure 5.15 shows the reconstruction error for each target and model as a function of the number of samples used in reconstruction. These are plotted with solid colored lines on the graphs. There is also a dashed black line marked on the graphs. This is a baseline error computed with Equation (5.2) using the raster scans discussed in Section 5.2 for $\hat{\boldsymbol{x}}$. This gives us a sense of the amount of misalignment between our truth image and the actual LED locations. In general, we do not expect the error to fall below this baseline, however, the raster scan can not account for spatial gradient effects in the mirror as we do in Model 4. This gives Model 4 the potential to beat our baseline error.

As expected, error generally reduces as the number of measurements increase. The exception to this, is when very few measurements are used in the reconstruction. If not enough measurements are used, the reconstruction can return an empty or nearly empty

signal. This empty signal will have a lower error compared to the highly noisy signal reconstructed when slightly more measurements are used. The normalized squared error may be lower for the empty signal, but that signal has not reconstructed any of the data present in the signal.

It is easy to see that the uncalibrated model 0 has significantly higher error than the calibrated models. Model 1 offers a significant reduction in reconstruction error compared to Model 0, and Models 2 and 3 moderately reduce error compared to Model 1. Model 3 itself is a very slight improvement from Model 2. These models appear to be close to functionally identical for our data. Model 4 is some what inconsistent. It reduces the error present in some of the signals and even beats the baseline error for the W target. However, it performs worse than Models 1-3 for the S target reconstruction particularly in the higher sample reconstructions. Note that in all cases the gradient Model 4 is still a significant improvement compared to the uncalibrated model and that the differences in error between Models 2 through 4 are very small. This matches our observations from the visual reconstruction results.

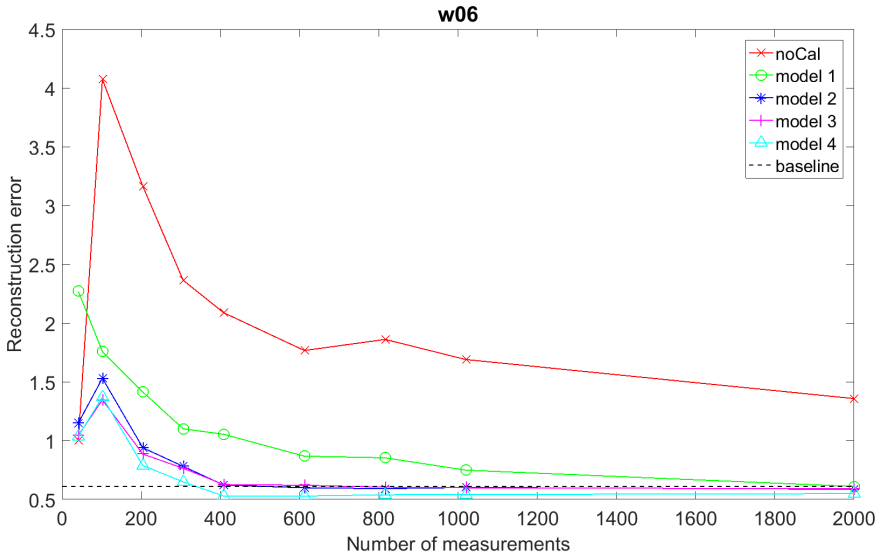

(a) Reconstruction error plot for W target

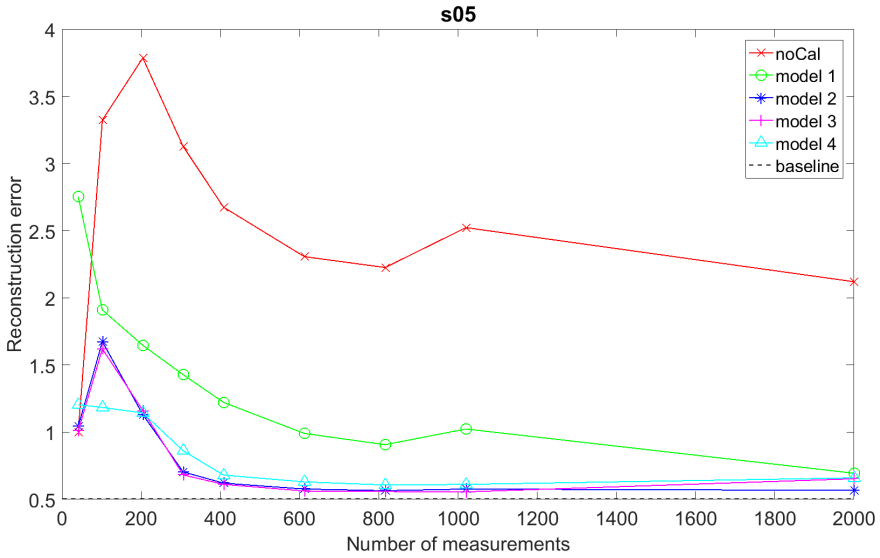

(b) Reconstruction error plot for S target

Figure 5.15: Reconstruction error plots

Conclusions

6.1 Summary of Contributions

We have developed an image acquisition system using a DMD to collect CS measurements. During the testing process, we discovered that the DMD degraded the signal and that modeling the measurement matrix as a series of ones and zeros was not adequate. We proposed three new calibration models to address issues introduced by the DMD and improve reconstruction results. We compare these new models with the uncalibrated data and a baseline model found in the CS literature. Our new calibration models can produce an adequate reconstruction using a number of measurements equal to only 20 percent of the signal length. The baseline and uncalibrated models still miss some points on our test targets when using 40 percent of the measurements. The new calibration models also produce more visually pleasing reconstructions with less noise.

There was only a small improvement in both the visual reconstruction and our error metric between Models 2 and 3. We believe that Model 3 would offer more substantial improvement if the ambient light in the testing environment was brighter (a higher β value) or if the expected number of on mirror changed between measurements. For our data set Models 2 and 3 performed equally.

Model 4 was introduced to address an intensity gradient observed in reconstructed images. We did observe more uniform intensities, particularity for the W test target. We believe that a more thorough collection of calibration data would improve these results.

6.2 Future Research

We developed an CS image acquisition system that could be used as a test bed. Since the target, DMD, and camera can all be easily and automatically controlled, this system can be used as a starting point to test additional calibration models, new algorithms, and new acquisition techniques. Possible areas worthy of additional exploration include trying DMD patterns more complex than ones and zeros, varying super mirror size, and adaptive pattern selection.

We were not able to collect ideal truth data for our calibration targets. We believe that ideal truth data could improve the calibration for gradient Model 4 and improve the accuracy of our estimated measurement matrix. We suggest that future experiments calculate a response for each LED in isolation as truth data. We also suggest collecting a series of calibration targets that equally cover all LEDs used in testing.

Bibliography

[1] R. M. Willett, R. F. Marcia, and J. Nichols, "Compressed sensing for practical optical imaging systems: a tutorial," in *Photonics Conference (IPC), 2012 IEEE*, pp. 586–586, IEEE, 2012.

[2] A. Mahalanobis, R. Shilling, R. Murphy, and R. Muise, "Recent results of medium wave infrared compressive sensing," *Applied Optics*, vol. 53, no. 34, pp. 8060–8070, 2014.

[3] M. Raginsky, R. M. Willett, Z. T. Harmany, and R. F. Marcia, "Compressed sensing performance bounds under poisson noise," *IEEE Transactions on Signal Processing*, vol. 58, pp. 3990–4002, Aug 2010.

[4] M. E. Gehm and D. J. Brady, "Compressive sensing in the EO/IR," *Appl. Opt.*, vol. 54, pp. C14–C22, Mar 2015.

[5] J. Bobin, J.-L. Starck, and R. Ottensamer, "Compressed sensing in astronomy," *IEEE Journal of Selected Topics in Signal Processing*, vol. 2, no. 5, pp. 718–726, 2008.

[6] C. Austin, J. Ash, and R. Moses, "Performance analysis of sparse 3D SAR imaging," in *Proc. SPIE, Algorithms for Synthetic Aperture Radar Imagery XVIII*, April 2011.

[7] J. Ash, "Joint imaging and change detection for robust exploitation in interrupted SAR environments.," in *Proc. SPIE, Algorithms for Synthetic Aperture Radar Imagery XX*, vol. 87460J, (Baltimore, MD), May 2013.

[8] A. Rich, L. Potter, N. Jin, J. Ash, O. Simonetti, and R. Ahmad, "A Bayesian model for highly accelerated phase-contrast MRI," *Magnetic Resonance in Medicine*, vol. 76, pp. 689–701, Aug. 2016.

[9] M. Lustig, D. Donoho, and J. M. Pauly, "Sparse MRI: The application of compressed sensing for rapid MR imaging," *Magnetic Resonance in Medicine*, vol. 58, no. 6, pp. 1182–1195, 2007.

[10] T. A. Basha, M. Akçakaya, B. Goddu, S. Berg, and R. Nezafat, "Accelerated three-dimensional cine phase contrast imaging using randomly undersampled echo planar imaging with compressed sensing reconstruction," *NMR in Biomedicine*, vol. 28, no. 1, pp. 30–39, 2015.

[11] V. Cambareri, A. Moshtaghpour, and L. Jacques, "A greedy blind calibration method for compressed sensing with unknown sensor gains," in *Information Theory (ISIT), 2017 IEEE International Symposium on*, pp. 1132–1136, IEEE, 2017.

[12] A. A. Wagadarikar, N. P. Pitsianis, X. Sun, and D. J. Brady, "Video rate spectral imaging using a coded aperture snapshot spectral imager," *Optics express*, vol. 17, no. 8, pp. 6368–6388, 2009.

[13] M. Wakin, J. Laska, M.Duarte, D. Baron, S. Sarvotham, D. Takhar, K.Kelly, and R. Baraniuk, "An architecture for compressive imaging," *Proc. International Conference on Image Processing*, 2006.

[14] D. Takhar, J. Laska, M. B. Wakin, M. F. Duarte, D. Baron, S. Sarvotham, K. Kelly, and R. G. Baraniuk, "A new compressive imaging camera architecture using optical-

domain compression," *IS&T/SPIE Computational Imaging IV*, vol. 6065, no. 606509, p. 1, 2006.

[15] R. H. Shepard, C. Fernandez-Cull, R. Raskar, B. Shi, C. Barsi, and H. Zhao, "Optical design and characterization of an advanced computational imaging system," Society of Photo-Optical Instrumentation Engineers (SPIE), 2014.

[16] Y. Wu, C. Chen, P. Ye, Z. Wang, G. Arce, and D. W. Prather, "Optical calibration of a Digital Micromirror Device (DMD)-based compressive imaging (CI) system," vol. 7210, 02 2009.

[17] E. J. Candès and M. B. Wakin, "An introduction to compressive sampling," *IEEE signal processing magazine*, vol. 25, no. 2, pp. 21–30, 2008.

[18] E. J. Candes and T. Tao, "Near-optimal signal recovery from random projections: Universal encoding strategies?," *IEEE transactions on information theory*, vol. 52, no. 12, pp. 5406–5425, 2006.

[19] D. L. Donoho, "Compressed sensing," *IEEE Transactions on information theory*, vol. 52, no. 4, pp. 1289–1306, 2006.

[20] J. A. Tropp and A. C. Gilbert, "Signal recovery from random measurements via orthogonal matching pursuit," *IEEE Transactions on information theory*, vol. 53, no. 12, pp. 4655–4666, 2007.

[21] D. Needell and R. Vershynin, "Uniform uncertainty principle and signal recovery via regularized orthogonal matching pursuit," *Foundations of computational mathematics*, vol. 9, no. 3, pp. 317–334, 2009.

[22] D. L. Donoho, Y. Tsaig, I. Drori, and J.-L. Starck, "Sparse solution of underdetermined systems of linear equations by stagewise orthogonal matching pursuit," *IEEE Transactions on Information Theory*, vol. 58, no. 2, pp. 1094–1121, 2012.

[23] S. Ji, Y. Xue, and L. Carin, "Bayesian compressive sensing," *IEEE Transactions on Signal Processing*, vol. 56, pp. 2346–2356, June 2008.

[24] M. E. Tipping and A. Faul, "Fast marginal likelihood maximisation for sparse Bayesian models.," in *Proceedings of the Ninth International Workshop on Artificial Intelligence and Statistics*, 2003.

[25] A. C. Faul and M. E. Tipping, "Analysis of sparse Bayesian learning," in *Advances in neural information processing systems*, pp. 383–389, 2002.

[26] S. M. Kay, *Fundamentals of statistical signal processing: Detection theory, vol. 2*. Prentice Hall, 1998.

[27] S. M. Kay, *Fundamentals of statistical signal processing: Estimation theory, vol. 1*. Prentice Hall, 1993.

[28] Y. Huang, J. L. Beck, S. Wu, and H. Li, "Robust bayesian compressive sensing for signals in structural health monitoring," *Computer-Aided Civil and Infrastructure Engineering*, vol. 29, no. 3, pp. 160–179, 2014.

[29] L. Carin, "Bayesian compresive sensing code," Duke University. Available at http://people.ee.duke.edu/~lcarin/BCS.html.

[30] C. of Southern Nevada, "LCD (Liquid Crystal Display) color monitor introduction."

[31] M. Fairchild and D. Wyble, "Colorimetric characterization of the apple studio display (flat panel lcd)," 1998.

[32] adafruit, "Medium 16x32 rgb led matrix panel product ID 420."

[33] S. Monk, "Connecting a 16x32 RGB LED matrix panel to a Raspberry Pi." Adafruit Learning System.

[34] H. Zeller, "Controlling RGB LED display with Raspberry Pi GPIO." Available at https://github.com/hzeller/rpi-rgb-led-matrix.

[35] Texas Instruments, *DLP6500FYE DMD Data Sheet*.

[36] Texas Instruments, *DLP LightCrafter 6500 and 9000 EVM User's Guide*.

[37] P. Mouroulis and J. Macdonald, *Geometrical optics and optical design*. Oxford University Press, USA, 1997.

[38] Allied Vision, *Prosilica GX 1050 Data Sheet*.

[39] Allied Vision, *Prosilica GX Technical Manual*.